# Insights into Global Glacier Dynamics Using Physics-Based Modelling

by

**Vivek Gajadhar**

# Insights into Global Glacier Dynamics Using Physics-Based Modelling

by

## Vivek Gajadhar

to obtain the degree of Master of Science

at the Delft University of Technology,

to be defended publicly in April 2024

An electronic version of this thesis is available at `http://repository.tudelft.nl/`.

# Acknowledgements

# Abstract

This thesis delves into glacier dynamics using the 2D Shallow Ice Approximation enriched by satellite remote sensing data on glacier surface velocities and ice thickness, aiming to refine empirical laws for better predicting glacier movements. The integration of such data has been pivotal, markedly enhancing model calibration despite challenges like steady-state assumptions necessitated by data scarcity. This underscores the critical role of high-quality, temporally resolved data in modeling glacier dynamics accurately. A significant advancement was the implementation of spatial stratification, which notably improved model performance—reducing Root Mean Square Error (RMSE) by up to 30% and elevating the coefficient of determination ($R^2$) by 0.2 to 0.4 across different regions. This highlights the potential of fully distributed inversions to capture the complex variability of glaciers. Employing Julia for its computational efficiency proved effective for large-scale modeling tasks, setting a promising foundation for future research aimed at understanding and predicting glacier responses to climate change. It is recommended to utilize geostatistical interpolation methods for inverting glacier characteristics from sparse data, in order to acquire these characteristics across the entire glacier area.

# Contents

# 1 Introduction

Glaciers serve as critical reservoirs of freshwater for human populations living in the contiguous plains of the world's largest mountain ranges, and exert a significant influence on global sea levels and ecosystems [1] [2]. Despite their importance, our understanding of glacier dynamics at large spatial and regional scales remains constrained [3]. This limitation arises from the intricate interactions between glaciers and both climatic and topographical factors, which are often not adequately captured in existing large scale glacier models [4]. Current studies frequently focus on individual glaciers with a high amount of observations, or conversely, lack the fine-grained analysis required for a comprehensive understanding of global glacier dynamics [5]. Such gaps in knowledge directly impact our ability to make accurate predictions concerning glacier ice volume changes, sea-level rise, and freshwater availability. These predictive shortcomings could, in turn, hamper policy decisions aimed at mitigating climate change and managing water resources sustainably [6].

The primary objective of this research is to enhance our understanding of glacier dynamics through the application of data driven, physics-based models. Specifically, this study utilises newly available datasets of glacier surface velocities and glacier ice thickness, obtained via large-scale remote sensing from satellites. By doing so, the research aims to discover new semi-empirical laws that can better represent various physical processes in regional to global glacier models, such as glacier ice rheology and the sliding of glaciers at their bedrock interface.

The driving research question for this study is: "How can the integration of newly available remote sensing data enhance the calibration of physics-based models for a better understanding of global glacier dynamics?" To answer this question, the research unfolds in calibrating glacier evolution models using available datasets, while employing inversion techniques.

The remainder of this thesis is structured as follows: Chapter 2 offers an exhaustive review of the theory used, Chapter 3 details the research methodology, Chapter 4 present the results and their analysis, and Chapter 5 concludes the study with recommendations for future research.

# 2 Theory

## 2.1 Basics of Glacier Dynamics

Glaciers are dynamic systems, their behavior is shaped by a complex interplay of physical processes and environmental conditions. This intricate foundation is crucial for predictive modeling, particularly in understanding how climate change impacts global sea levels. The dynamics of glaciers emerge from multiple interrelated factors, each contributing in its own way.

**Accumulation and Ablation**
Accumulation and ablation are fundamental processes that dictate the mass balance of a glacier. These indicate the mass gained by the glacier via processes of accummulation, and the mass removed from the glacier via processes of ablation. Accumulation predominantly occurs through snowfall, while ablation includes processes like melting, evaporation, and calving (breaking of ice chunks at the edges). The mass balance, calculated as the difference between accumulation and ablation, serves as a vital indicator of glacier health and stability [7].

**Creep**
Internal deformation or creep, is akin to the flow observed in viscous fluids. This internal deformation is crucial for understanding glacier movements, as it mirrors the behavior of such fluids under varying pressures and temperatures. To accurately describe and predict this phenomenon, scientists rely on fluid dynamics equations, notably the Navier-Stokes equations (see chapter 2.2). These equations adeptly illustrate the complex, non-linear interplay between stress and strain rates within glaciers, providing a comprehensive framework for analyzing glacier flow mechanisms [8].

**Basal Sliding**
In addition to internal deformation, basal sliding occurs due to water flow or softer sediment at the glacier bed. Both reduce basal friction and allows faster ice flow. This phenomenon can significantly contribute to the overall movement of glaciers and needs to be accounted for in any comprehensive glacier model. [9].

**Surface and Bed Topography**
The topographical characteristics of a glacier's surface significantly influence ice flow patterns. It's the surface topography (top of the glacier) or gradient that primarily drives ice flow, rather than the basal topography (bottom of the glacier). Accurate topographical data are indispensable for realistic glacier modeling. [10].

**Feedback Mechanisms**
Glaciers are sensitive indicators of climate change, with dynamics closely linked to atmospheric conditions. Temperature and precipitation fluctuations affect accumulation and ablation rates, impacting the glacier's mass balance [11]. Feedback mechanisms, such as changes in albedo, amplify these effects. Melting decreases surface albedo, leading to increased absorption of solar radiation and further melting [12]. Glacier dynamics are intricately tied to elevation and glacier geometry. Elevation affects how glaciers experience climate, with those at higher elevations exposed to different conditions than lower ones, influencing their mass balance over time. Glacier geometry, including shape and size, dictates response to climatic changes, crucial for accurate future projections [13].

## 2.2 Governing Equations for Ice Flow

### 2.2.1 Navier-Stokes Equations

In glacier dynamics, understanding the flow behavior of ice is crucial. Glacier ice behaves as a viscous, incompressible fluid over longer timescales and larger spatial scales. The Navier Stokes equations, which are a set of governing equations, describe the flow of such substances. They are derived from the fundamental principles of conservation of momentum and mass for a continuum medium [14] [15]. The momentum balance equation, representing the balance between the driving forces and resistive stresses, is:

$$\rho \left( \frac{\partial \mathbf{u}}{\partial t} + \mathbf{u} \cdot \nabla \mathbf{u} \right) = -\nabla p + \nabla \cdot \boldsymbol{\tau} + \rho \mathbf{g} \tag{1}$$

Meanwhile, the continuity equation is:

$$\frac{\partial \rho}{\partial t} + \nabla \cdot (\rho \mathbf{u}) = 0 \tag{2}$$

In these equations:

- $\boldsymbol{\tau}$ [Pa] is the deviatoric stress tensor , which quantifies the differential stresses within the ice.

- $\mathbf{u}$ [m/s] is the velocity vector, representing how fast and in which direction the ice is flowing.

- $\rho$ [kg/m$^3$] is the ice density, a measure of how much mass of ice is present in a given volume.

- $\mathbf{g}$ [m/s$^2$] is the acceleration due to gravity, which acts as a primary driving force for glacier flow, especially in steep terrains.

- $p$ [Pa] is the pressure in the ice, influencing the direction and rate of its flow. It prompts movement from areas of high to low pressure.

Two key assumptions for ice flow are:

- **Incompressibility:** Glacier ice is nearly incompressible, implying a consistent density in time and space. Ice's near incompressibility arises from its hexagonal crystalline lattice, formed by water molecules interconnected by strong hydrogen bonds. This structure resists substantial volume changes under pressure [16]. Notice that at the top of a glacier this is not necessarily true due to for example snowfall.

- **Slow ice flow:** The glacier's slow movement allows the neglect of inertial terms [17]. This is evident from the dimensionless Reynolds number, which characterizes the flow regime in fluids by indicating the ratio between inertial and viscous forces [18].

$$\mathrm{Re} = \frac{\rho U L}{\mu} \tag{3}$$

With:

- $\rho$: The density of the ice.

- $U$: The characteristic velocity, representing the typical speed at which the glacier ice flows.

- $L$: The characteristic length scale, often representing the thickness or another relevant dimension of the glacier.

- $\mu$: The dynamic viscosity, indicating the resistance of the glacier ice to deformation and flow.

With $L \approx 100$ m, $U \approx 10^{-6}$ m/s, $\rho \approx 10^3$ kg/m$^3$, and $\mu \approx 10^{12}$ Pa $\cdot$ s, Re is roughly $10^{-13}$ [17] [19]. Re « 1, which means that inertial forces are very small compared to the gravitational and viscous forces, leading to a flow governed by gravity, pressure gradients, and viscosity.

Using the two above assumptions, equations 1 and 2 reduce to:

$$0 = -\nabla p + \nabla \cdot \boldsymbol{\tau} + \rho \mathbf{g} \tag{4}$$

$$\nabla \cdot \mathbf{u} = 0 \tag{5}$$

### 2.2.2 Boundary Conditions

In glacier physics, boundary conditions are important to accurately solving the Navier-Stokes equations. It's crucial to distinguish between two main types of boundaries: prescribed and free. The glacier bed is typically a prescribed boundary, while the upper surface is a free boundary, due to negligible friction between ice and air. For floating ice shelves, both the lower and upper surfaces, including the calving front, are free boundaries [20].

At prescribed boundaries, conditions on the velocity components are imposed. In contrast, free boundaries require the imposition of both kinematic and dynamic conditions. These conditions are essential to determine the location or movement of the boundaries.

**The No-Slip Condition and the Sliding Law:**

For viscous fluids at a rigid boundary, the usual condition is the no-slip condition. This implies that the fluid moves congruently with the boundary's prescribed velocity. Mathematically, this is represented as:

$$\boldsymbol{u} \cdot \boldsymbol{n} = u_n \tag{6}$$

$$\boldsymbol{u} - (\boldsymbol{u} \cdot \boldsymbol{n})\boldsymbol{n} = \boldsymbol{u_b} \tag{7}$$

where $\boldsymbol{n}$ is the upward-pointing unit normal to the bed, $u_n$ is the normal velocity at the boundary, and $\boldsymbol{u_b}$ is the tangential velocity vector [21].

When the bed reaches the melting point, a thin water layer can result in slip. This can generally be described by a sliding law, which links the tangential velocity (velocity due to sliding) of the ice to the local shear stress:

$$\boldsymbol{u_b} = \frac{F(\tau_b)\boldsymbol{\tau_b}}{\tau_b} \tag{8}$$

Here, $\boldsymbol{u_b}$ denotes the vector of the tangential velocity and $\boldsymbol{\tau_b}$ is the vector of the basal shear stress, while $\tau_b$ represents its magnitude [20]. Note that the function $F(\tau_b)$ in the sliding law equation is not explicitly defined, accommodating different models like Weertman's law which relates sliding velocity to the basal shear stress raised to a power ($F(\tau_b) = C\tau_b^m$) [22].

Furthermore, if melting occurs at the bed, the no-penetration condition should account for potential mass loss at the bed:

$$\boldsymbol{u} \cdot \boldsymbol{n} = -m_b \tag{9}$$

where $m_b$ is the basal melt rate.

**Dynamic Boundary Conditions:**

At a free surface, the stress on the boundary, $\boldsymbol{\tau} \cdot \boldsymbol{n}$, matches the stress from the surrounding material. Typically, this is either air or ocean (water) [20]. This is given by:

$$\boldsymbol{\tau} \cdot \boldsymbol{n} = -p_b \boldsymbol{n} \tag{10}$$

On a glacier's upper surface, $p_b$ equals the atmospheric pressure $p_a$. In the ocean, it's defined by the equation:

$$p_b = p_a - \rho_w g z \tag{11}$$

where $z$ is the vertical coordinate relative to sea level and $\rho_w$ is the ocean water density.

**Kinematic Boundary Conditions:**

For free boundaries comprising the same fluid parcels consistently, the kinematic condition demand that the fluid on the boundary moves synchronously with the boundary's velocity. This is in fact the same as the no-slip condition described in equations 6 and 7 [21].

In the glaciological context, the free boundary is often denoted as:

$$z = s(x, y, t) \tag{12}$$

where $s$ is the upper surface of the glacier. The following condition is obtained, when differentiating both sides of the above equation with respect to time:

$$u_z = \frac{\partial s}{\partial t} + u_x \frac{\partial s}{\partial x} + u_y \frac{\partial s}{\partial y} \tag{13}$$

When mass is either added to or removed from a boundary over time, the kinematic condition becomes:

$$u_n = \boldsymbol{u} \cdot \boldsymbol{n} + a_n \tag{14}$$

Here, $a_n$ represents the normal rate of mass addition or subtraction. In situations where the fluid is stationary, the boundary moves at this rate. Conversely, when fluid transport away from the boundary matches the rate $a_n$, the boundary remains stationary.

Transforming the above relation, the following is obtained:

$$\frac{\partial s}{\partial t} + u_x \frac{\partial s}{\partial x} + u_y \frac{\partial s}{\partial y} = u_z + a \tag{15}$$

In this context, $a$ is the vertical accumulation rate, which is a function of $a_n$ and the inclination of the boundary. Specifically:

$$a = \frac{a_n}{\sqrt{1 + \left(\frac{\partial s}{\partial x}\right)^2 + \left(\frac{\partial s}{\partial y}\right)^2}} \tag{16}$$

Given the typical near-vertical orientation of glacier boundaries, the difference between $a$ and $a_n$ is usually minor [21].

### 2.2.3 Temperature and Energy Conservation

Conservation of energy in ice flow is constructed analogously to momentum conservation. Considering a specified volume $V$ of a glacier, both its internal energy $e$ and kinetic energy are accounted for. The kinetic energy component is very small compared to the internal energy due to the slow movement characteristic of glaciers and ice sheets and can be omitted [15] [20], however it is retained for consistency.

Energy variations within the volume $V$ result from mass advection and its associated energy in and out of $V$, heat conduction as dictated by Fourier's law with conductivity $k$, and work exerted by external forces [20].

Mathematically, energy conservation takes the form:

$$
\begin{aligned}
\frac{d}{dt} \int_V \rho \left(e + \frac{1}{2}|\boldsymbol{u}|^2\right) dV = & -\int_{\partial V} \rho \left(e + \frac{1}{2}|\boldsymbol{u}|^2\right) \boldsymbol{u} \cdot \boldsymbol{n} dS \\
& + \int_{\partial V} k \nabla T \cdot \boldsymbol{n} dS \\
& + \int_V \rho \boldsymbol{u} \cdot \boldsymbol{g} dV \\
& + \int_{\partial V} \boldsymbol{u} \cdot (\boldsymbol{\tau} \cdot \boldsymbol{n}) dS.
\end{aligned}
\tag{17}
$$

In the above equation, the term on the left side denotes the rate of change of total energy within $V$, encompassing the sum of internal and kinetic energies. On the right side the first term represents energy outflow from $V$ due to advection. The second term quantifies the total heat conducted across the boundary of $V$ due to Fourier's law. The third term aggregates the gravitational work over the entire volume $V$, and the last term signifies the work by the stress tensor on fluid elements crossing the boundary $\partial V$.

By using Reynolds transport theorem [23], Divergence theorem [24], the momentum equation (equation 1), the continuity equation (equation 2) and the thermodynamic relation $\frac{De}{Dt} = c_p \frac{DT}{Dt}$ (where $c_p$ represents the specific heat capacity and $\frac{D}{Dt}$ being the material derivative) [25], the following equation can be derived:

$$\rho c_p \left( \frac{\partial T}{\partial t} + \boldsymbol{u} \cdot \nabla T \right) = \nabla \cdot (k \nabla T) + \tau_{ij} \dot{\epsilon}_{ij}. \tag{18}$$

The full derivation of the above equation can be found in Appendix A.

**Boundary Conditions**

For the energy equation, boundary conditions vary based on the situation. In instances where the upper and basal glacier surfaces remain below the melting point throughout the year, the upper surface temperature aligns with the mean annual air temperature $T_a$, and the temperature gradient at the base is offset by the geothermal heat flux $G$. When the glacier's surface, base, or internal temperature meets the melting point $T_m$, the condition becomes $T = T_m$. If the internal temperature of the ice reaches $T_m$, the energy equation accommodates latent heat effects due to potential internal melting [20].

## 2.3 Glen's Flow Law and Non-Newtonian Behavior of Ice

Glacier ice exhibits non-linear viscous behavior, distinguishing it from the linear behavior observed in Newtonian fluids such as air or water. This non-linearity in ice deformation is empirically described by Glen's flow law, which was developed based on experiments where ice samples were subjected to varying stress conditions, and the resulting strain rates were measured [26].

For a Newtonian fluid, the relationship between stress and strain rate is linear and is given by:

$$\tau_{ij} = 2\mu \dot{\epsilon}_{ij} \tag{19}$$

Where $\mu$ is a constant viscosity. The strain rate tensor $\dot{\epsilon}$ is defined as:

$$\dot{\epsilon}_{ij} = \frac{1}{2} \left( \frac{\partial u_i}{\partial x_j} + \frac{\partial u_j}{\partial x_i} \right) \tag{20}$$

However, in the case of glacier ice, the strain rate $\dot{\epsilon}$ is not directly proportional to the applied deviatoric stress $\tau$. Instead, it relates through Glen's power-law:

$$\dot{\epsilon}_{ij} = A\tau^{n-1}\tau_{ij}, \qquad \tau = \sqrt{\frac{1}{2}\tau_{ij}\tau_{ij}} \tag{21}$$

Where $\tau$ is the second invariant of the stress tensor, indicating the effective stress; $A$ is a flow parameter influenced by factors such as temperature, grain size, and impurities; and $n$ is the stress exponent. Empirical observations have typically found $n \approx 3$, although this can vary under specific conditions [27].

Given the non-linear behavior of ice, the concept of an effective viscosity $\mu_{\text{eff}}$ is introduced. This effective viscosity, unlike the constant viscosity of Newtonian fluids, is dependent on the applied stress or strain rate. Derived from equations 19 and 21, the effective viscosity is given by:

$$\mu_{\text{eff}} = \frac{1}{2A\tau^{n-1}} \tag{22}$$

Thus, Glen's flow law for ice can be seen as a modification of the Newtonian relationship, using an effective viscosity that varies with the effective strain rate:

$$\tau_{ij} = A^{-\frac{1}{n}}\dot{\epsilon}^{\frac{1-n}{n}}\dot{\epsilon}_{ij}, \qquad \dot{\epsilon} = \sqrt{\frac{1}{2}\dot{\epsilon}_{ij}\dot{\epsilon}_{ij}} \tag{23}$$

,

The flow-law rate constant $A(T)$ has a temperature dependency, thus coupling the solution to the Stokes equations (equations 1 and 2) for ice velocity with the energy equation (equation 18). However, for simplification, the temperature dependence of $A$ is often neglected [28].

## 2.4 Shallow Ice Approximation

The Shallow Ice Approximation (SIA) is a fundamental approach for simulating ice flow, especially when considering that the aspect ratio of the flow is large. This means that variations in the horizontal coordinate are much smaller than those in the vertical, making SIA a suitable model especially for grounded ice that does not slide too rapidly. However, it is worth noting that ice shelves and rapidly moving ice streams are not properly described by this model [29] [30].

At the heart of the SIA lies its capacity to simplify the full Stokes equations governing glacier flows. This is achieved by focusing on the most influential terms and neglecting others of lesser impact. Specifically, the SIA concentrates on the vertical shear stress components $\tau_{xz}$ and $\tau_{yz}$ while ignoring other components of the deviatoric stress tensor [29] [31].

Under these conditions, the momentum equations and surface boundary conditions can be approximated as:

$$-\frac{\partial p}{\partial x} + \frac{\partial \tau_{xz}}{\partial z} = 0,$$
$$-\frac{\partial p}{\partial y} + \frac{\partial \tau_{yz}}{\partial z} = 0,$$
$$-\frac{\partial p}{\partial z} - \rho g = 0,$$
$$p = \tau_{xz} = \tau_{yz} = 0 \text{ at } z = s(x, y, t). \tag{24}$$

Leading to:

$$p = \rho g(s - z),$$
$$\begin{pmatrix} \tau_{xz} \\ \tau_{yz} \end{pmatrix} = -\rho g(s - z)\nabla s. \tag{25}$$

where $\nabla$ is the two-dimensional gradient.

Using the found relations for $\tau_{xz}$ and $\tau_{yz}$ and Glen's flow law as described in equation 21, the deformation can be described as:

$$\begin{bmatrix} \frac{\partial u_x}{\partial z} \\ \frac{\partial u_y}{\partial z} \end{bmatrix} = -2A(\rho g)^n (s - z)^n |\nabla s|^{n-1} \nabla s \tag{26}$$

Integrating the above relationship from the bed $b$ to a point $z$ below the surface gives:

$$\mathbf{u}_d = -\frac{2A(\rho g)^n}{n + 1} \left[ h^{n+1} - (s - z)^{n+1} \right] |\nabla s|^{n-1} \nabla s \tag{27}$$

where $\mathbf{u}_d$ describes the contribution to the velocity due to deformation and $h = s - b$ is the ice thickness.

Since the basal shear stress is in the same direction as $\nabla s$, the sliding law (equation 8), can be expressed as:

$$\boldsymbol{u_b} = F(\tau_b)|\nabla s|^{-1}\nabla s \tag{28}$$

where $\tau_b = |\rho g h \nabla s|$ is the basal shear stress.

The total horizontal velocity (in the x and y directions) is then the sum of the velocities due to sliding and deformation:

$$\mathbf{u} = \boldsymbol{u_b} + \mathbf{u}_d \tag{29}$$

Combining equation 27 and 28 results in:

$$\boldsymbol{u} = -F(\tau_b)|\nabla s|^{-1}\nabla s - \frac{2A(\rho g)^n}{n+1}\left[h^{n+1} - (s-z)^{n+1}\right]|\nabla s|^{n-1}\nabla s \tag{30}$$

The depth-integrated ice flux, $q$, is then given by:

$$\boldsymbol{q} = \int_b^s \boldsymbol{u}\,dz = -F(\tau_b)h|\nabla s|^{-1}\nabla s - \frac{2A(\rho g)^n}{n+2}h^{n+2}|\nabla s|^{n-1}\nabla s \tag{31}$$

This represents the combination of ice flux due to sliding and the shearing velocity profile in the ice [29].

The rate of change of the ice mass $\frac{\partial M}{\partial t}$ is influenced by the net flow of ice into or out of the element, represented by the divergence of the ice flux $\nabla \cdot q$, and the local accumulation or ablation rate $\dot{a}$.

Using the above considerations and $M = \rho A h$, the mass conservation for the glacier is expressed as:

$$\frac{\partial h}{\partial t} = \dot{a} + \nabla \cdot \left(F(\tau_b)h|\nabla s|^{-1}\nabla s + \frac{2A(\rho g)^n}{n+2}h^{n+2}|\nabla s|^{n-1}\nabla s\right) \tag{32}$$

This equation captures the balance of processes affecting ice thickness in a glacier.

# 3 Methods

## 3.1 ODINN.jl

Within the ambition of enhancing glacier modeling techniques, this research contributes to the `ODINN.jl` project, a framework that integrates the Open Global Glacier Model (OGGM) with Universal Differential Equations [32] [33]. This collaboration aims to refine the understanding of glacier processes through a combination of mechanistic modeling and machine learning. Through this contribution, the research not only aims to advance the understanding of glacier dynamics but also contributes to a potential of combining traditional modeling techniques with the latest advancements in machine learning.

The project utilizes OGGM [34] to gather topographical and climatic data, establishing the initial conditions for glacier simulations. By invoking Python libraries within Julia, `ODINN.jl` benefits from integration of the comprehensive data collection capabilities of OGGM and the advanced computational efficiency of Julia. This approach enables high-performance simulations that are crucial for modeling the intricate interactions between glaciers and climate change.

## 3.2 Scientific Computing using Julia

For this research Julia was selected as programming language. Julia stands out due to its unique combination of features tailored for scientific computing. It combines the speed of languages like C and Fortran with a user-friendly coding environment [35]. A key advantage of Julia is its automatic differentiation (AD) feature, which is essential for modern scientific modeling. AD is applied within this research (see chapter 3.7.2) ,because it facilitates the accurate and efficient computation of gradients, crucial for model optimization and solving inverse problems [36].

The Julia ecosystem is enriched with a vast array of packages covering various scientific domains, such as `DifferentialEquations.jl`, `Optimization.jl`, and `Makie.jl` (data visualization)[37] [38] [39].

Interoperability is another significant aspect of Julia, enabling easy integration with other programming languages and thereby expanding its application scope. For example it is possible to access Python language and packages within the Julia environment (e.g. OGGM). The Julia community plays a pivotal role in the language's success, providing extensive documentation and support.

## 3.3    Inversion Method

Inversion techniques play an important role in determining unknown parameters of a model by minimizing the difference between model predictions and observed data. In the context of glaciers, observed surface velocities and ice thickness often serve as data to inform glacier ice flow model parameters.

Inversion's main benefit is its ability to incorporate actual field observations of glacier behavior directly into model refinement, avoiding reliance on laboratory measurements or assumptions. It begins with data collection, followed by constructing a predictive model, quantifying discrepancies through an objective function, optimizing parameters to minimize these discrepancies, and validating the improved model against independent datasets. See the following list for an overview of the elements in an inversion process:

1. **Data Collection**: Gather observational data, such as surface velocities or ice thickness of the glacier, through methods like satellite remote sensing or ground-based measurements.

2. **Forward Model**: Construct a forward model predicting glacier behavior based on initial conditions and parameters.

3. **Objective Function**: Formulate an objective function that quantifies discrepancies between the forward model's predictions and observational data. A prevalent choice is the mean squared error between observed and predicted quantities.

4. **Optimization**: Apply optimization algorithms to minimize the objective function by adjusting model parameters. This iterative cycle persists until the parameters converge to values that are consistent with both model predictions and observational data. Gradients are critical for optimization because they guide the algorithms toward the minimum of the objective function by indicating the direction in which parameters should be adjusted to reduce discrepancies between model predictions and observational data.

5. **Validation**: Apply derived parameters to predict glacier behaviors in various scenarios or regions and compare these predictions to independent datasets.

## 3.4    Observational Data Sources

For a comprehensive understanding of glacier dynamics, this study employs datasets from the following sources:

**Millan et al. (2022)**: Global glacier ice surface velocities of glaciers from this study are determined by processing data from optical sensors (e.g., Sentinel-2, Landsat 7/8, Pléiades) using an automated workflow that includes feature tracking and calibration techniques to produce precise, time-averaged velocity maps [40]. Available through the OGGM Python Library.

**GlaThiDa Consortium (2020)**: GlaThiDa (Glacier Thickness Database) is a comprehensive repository of glacier thickness measurements gathered from various global locations. Compiled by different research groups using diverse techniques, this database serves as a valuable resource for glacier research [41].

**Various sources (2000-2018)**: Digital Elevation Maps (DEMs) provide foundational data for modeling glacier and ice dynamics. Available from a variety of sources (e.g. SRTM [42] & DEM3 [43]) through OGGM, these maps offer insights into terrain elevations essential for accurate simulations of glacier behavior and changes over time.

**Farinotti et al. (2019)**: Offers inverted ice thicknesses of about 215,000 global glaciers, excluding Greenland and Antarctic sheets, by integrating up to five models using DEMs and ice flow dynamics. [44]. The resulting data are accessible through the OGGM Python Library.

The OGGM framework additionally offers access to a diverse array of glacier-related information, including, among others, distance to borders, longitude and latitude coordinates, slope, and actual pixel width.

## 3.5 Forward Model

The forward model employed in this research is based on modifying the SIA equation for the ice thickness (see equation 32) [32]. The modeling of basal sliding, $F(\tau_b)$, in this research is done using zeroth order Weertman's law [22], $F(\tau_b) = C$, which leads to:

$$\frac{\partial h}{\partial t} = \dot{a} + \nabla \cdot \left( Ch|\nabla s|^{-1}\nabla s + \frac{2A}{n+2}(\rho g)^n h^{n+2}\|\nabla s\|^{n-1}\nabla s \right) \tag{33}$$

In the equation above:

- $\dot{a}$ is the surface mass balance

- $C$ denotes the basal sliding coefficient.

- $\nabla s$ represents the surface gradient.

- $A$ is the flow rate factor, which accounts for ice rheology and temperature dependencies.

- $\rho$ stands for ice density.

- $g$ is the gravitational acceleration.

- $n$ is the Glen's flow law exponent.

- $h$ represents the ice thickness.

The surface ice velocity can be determined via the ice thickness $h$ using equation 30 ($s - z = 0$ at surface), which leads to:

$$\boldsymbol{u} = -C|\nabla s|^{-1}\nabla s - \frac{2A(\rho g)^n}{n+1}h^{n+1}|\nabla s|^{n-1}\nabla s \tag{34}$$

The equation for calculating ice thickness based on ice surface velocity, is then as follows:

$$h = \left( \frac{|\boldsymbol{u}| + C}{\Gamma^*|\nabla s|^n} \right)^{\frac{1}{n+1}}, \Gamma^* = \frac{2A(\rho g)^n}{n+1} \tag{35}$$

## 3.6 Cost Function in Glacier Modeling

The cost function, remains foundational in inversion methodologies. It quantifies discrepancies between model predictions and observational data. The Mean Squared Error (MSE) serves as a method to structure this cost function:

$$\text{MSE} = \frac{1}{N} \sum_{i=1}^{N} (x_{\text{obs}_i} - x_{\text{pred}_i})^2 \tag{36}$$

In this equation, $x_{\text{obs}}$ denotes observed quantity of interest and $x_{\text{pred}}$ signifies predicted quantity of interest from the model. The quantity of interest could be either ice thickness or surface velocity in this context.

Within the context of glacier modeling, the squared term of the MSE ensures that large deviations between observed and predicted velocities contribute disproportionately to the total error. This penalization of larger errors is consistent with the desire to have a model that doesn't just get the "average" behavior right, but also accurately predicts the more extreme or outlier behaviors of glaciers. Additionally, its differentiability makes it particularly suitable for optimization methods [45].

However, MSE is not without its challenges. It may disproportionately respond to outliers, such as abnormal ice thickness measurements or velocity spikes, which can mislead the evaluation of model performance in capturing glacier dynamics. Despite these drawback, MSE's straightforwardness, ease of interpretation, and compatibility with optimization algorithms still make it a popular metric for regression tasks in glaciological studies [46].

## 3.7 Optimization Technique

### 3.7.1 BFGS optimization

BFGS is an optimization algorithm useful for minimizing cost functions. It is a quasi-Newton method that approximates the Hessian matrix to find a function's minimum, improving upon gradient descent by utilizing second-order derivative information. This results in faster convergence, making it efficient for complex problems where first-order methods are less effective [47].

The update formula is:

$$\mathbf{x}_{n+1} = \mathbf{x}_n - \gamma H_n^{-1} \nabla F(\mathbf{x}_n), \tag{37}$$

where $\mathbf{x}_n$ is the parameter vector at iteration $n$, $\gamma$ the step size, $H_n^{-1}$ the inverse Hessian approximation, and $\nabla F(\mathbf{x}_n)$ the gradient of $F$ at $\mathbf{x}_n$.

For glacier inversion, BFGS is particularly useful because it can efficiently navigate complex cost landscapes, typical in modeling glacier dynamics. The algorithm's ability to quickly converge with fewer iterations than gradient descent methods reduces computational time and resources, essential for handling the large datasets often encountered in glacier studies [48].

### 3.7.2 Derivative Calculation

Optimizing model parameters is crucial for glacier inversion methodologies, requiring accurate gradient computation to direct parameter adjustments and minimize model error. Automatic Differentiation (AD), efficiently computes these gradients by exploiting the computational graph of functions and the chain rule. Forward Mode AD is optimal for cases with fewer parameters, applying the chain rule across elementary functions. For situations with many parameters, like distributed optimizations or neural networks, Reverse Mode Differentiation is preferred due to its efficiency in differentiating with respect to a large number of parameters [49] [50]. Both modes are available in `ODINN.jl`, however in this research only Forward Mode AD is used.

**Dual Numbers**

Dual numbers offers an extension to conventional numerical variables by incorporating derivative information with respect to a certain parameter. A dual number consists of a value coordinate $x_1$ and a derivative coordinate $x_2$, where $x_2$ represents the derivative of $x_1$ with respect to the parameter $\theta$. This can be formally expressed as $x_\epsilon = x_1 + \epsilon x_2$, where $\epsilon$ is a element satisfying $\epsilon^2 = 0$ but $\epsilon \neq 0$.

The arithmetic of dual numbers, including addition and multiplication, is extended from real numbers by leveraging the property $\epsilon^2 = 0$. For instance, given two dual numbers $x_\epsilon = x_1 + \epsilon x_2$ and $y_\epsilon = y_1 + \epsilon y_2$, their sum and product are given by:

$$x_\epsilon + y_\epsilon = (x_1 + y_1) + \epsilon(x_2 + y_2) \tag{38}$$

$$x_\epsilon \cdot y_\epsilon = x_1 y_1 + \epsilon(x_1 y_2 + x_2 y_1) \tag{39}$$

Dual numbers are instrumental in implementing forward mode automatic differentiation, as they efficiently compute first-order derivatives by simulating infinitesimal perturbations in the Taylor series expansion of functions.

**Computational Graphs**

The computational graph serves as a foundational concept in automatic differentiation, providing a visual representation of the function evaluation process. This graph delineates each computational step as a node, with edges illustrating the flow of data from inputs through intermediate calculations to the final output. Such a structure not only clarifies the function evaluation sequence but also lays the groundwork for integrating derivative computations seamlessly into the process [51].

Consider a function $f(x) = \sin(7x)$, the evaluation follows a sequence of multiplying an input $x_1$ with 7 and then applying the sine function, culminating in the function's value at that point. The computational graph for this function depicts each evaluation stage, from input through intermediate operations to the final output. An accompanying graph for the derivative can be drawn as well, which helps to visualize how the derivatives are carried through. These graphs can be visualized as in Figure 1.
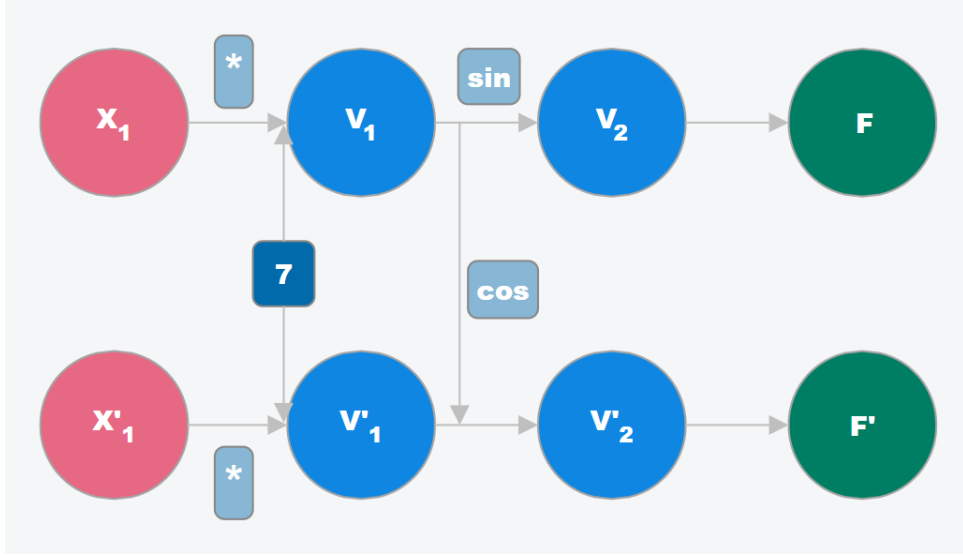
Figure 1: Computational and accompanying derivative graph of $f(x) = \sin(7x)$.

In Figure 1 the top portion of the graph outlines the forward pass. Simultaneously, the bottom portion of the graph traces the backward pass for the derivative. It starts with the derivative, which is then scaled by 7 (the derivative of $v_1$ with respect to $x_1$) to get $v_1'$. The chain rule is applied next, where the cosine of $v_1$ (the derivative of the sine function) is multiplied by $v_1'$ to determine $v_2'$. This results in the derivative of the final output $F'$. demonstrating how gradients are propagated through the graph.

Computational graphs can be extended to multiple variables. Consider $v_1, v_2, \ldots, v_p$ as the input variables; let $v_{p+1}, \ldots, v_{m-1}$ represent the intermediate variables, and $v_m$ symbolize the final output. This arrangement is strictly ordered such that each variable $v_i$ is the result of a function dependent solely on preceding variables $v_j$ where $j < i$.

Upon establishing the computational graph, the derivative of each node, can be computed utilizing the Bauer formula [52]:

$$\frac{\partial v_j}{\partial v_i} = \sum_{\substack{\text{paths } w_0 \to w_1 \to \ldots \to w_K \\ \text{with } w_0 = v_i, w_K = v_j}} \prod_{k=0}^{K-1} \frac{\partial w_{k+1}}{\partial w_k}, \tag{40}$$

The summation extends over all directed paths connecting an input to a target node within the graph. To streamline computations, one can progressively calculate $j = p+1, \ldots, m$ using the recursive relationship:

$$\frac{\partial v_j}{\partial v_i} = \sum_{w \to v_j} \frac{\partial v_j}{\partial w} \frac{\partial w}{\partial v_i}, \tag{41}$$

Here, each variable node $w$ leading to $v_j$ represents an edge in the computational graph and possesses an index smaller than $j$. This recursive process can be iterated synchronously with the program's execution to determine both the function's value and its gradient. The feasibility

16

of this method in forward mode arises from the fact that the term $\frac{\partial w}{\partial v_i}$ is already computed in a preceding iteration, while $\frac{\partial v_j}{\partial w}$ is computed concurrently as the node $v_j$ is evaluated, using only the values from its parent nodes. Differentiation thus hinges on the ability to calculate the derivative of each edge and to coalesce these via the given recursion.

### 3.7.3 Spatial Stratification Optimization

Initially, a simplified approach by inverting a single parameter across the entire glacier was attempted. However, this method failed to capture the complex spatial variability, leading to inadequate model performance. Recognizing the limitations of the initial approach and constrained by the current capabilities of the modeling architecture, a fully distributed inversion that would assign a unique parameter value to each grid pixel using Forward Mode AD, could not be implemented.

Ideally, one would want to perform an inversion with a value for each glacier grid cell. However, optimizing such a large number of parameters would require using reverse differentiation. Since this type of differentiation is still being implemented in the ODINN.jl architecture, we had to be creative and find a workaround compatible with forward differentiation, which is limited to a reduced number of parameters. The proposed solution was to cluster pixels into zones based on shared characteristics, such as altitude and proximity to the glacier's edge. This method allowed us to approximate the spatial variability of the glacier more effectively than a uniform parameter approach could. The glacier were divided into zones by altitude, further subdividing each altitude zone based on distance from the glacier border. This solution strikes a balance between the capabilities of Forward Mode AD and the spatial distribution needed for the inversion. However ultimately the inversion should be done in a fully distributed manner using Reverse Mode AD.

To demonstrate how the proposed solution works, consider dividing the glacier into regions based on altitude ($n = 2$) and distance to the border ($m = 2$). Let $H(x, y)$ denote the altitude of a pixel at coordinates $(x, y)$ and $D_{border}(x, y)$ denote the distance of the pixel from the glacier's border. The glacier can then be segmented into the following regions:

- Region 1: Pixels where $H(x, y) < 0.5 H_{\max}$, further subdivided into:
  - Region 1.1: Pixels with $D_{border}(x, y) < 0.5 D_{border,max}$.
  - Region 1.2: Pixels with $D_{border}(x, y) \geq 0.5 D_{border,max}$.
- Region 2: Pixels where $H(x, y) \geq 0.5 H_{\max}$, similarly subdivided into:
  - Region 2.1: Pixels with $D_{border}(x, y) < 0.5 D_{border,max}$.
  - Region 2.2: Pixels with $D_{border}(x, y) \geq 0.5 D_{border,max}$.

This scheme assigns each pixel $(x, y)$ to a specific region based on its altitude and distance to the border, effectively capturing the spatial variability of the glacier. Notice when optimizing $k$ different parameters (e.g. $A, n, C$), the total amount of parameters that need to be optimized is $k \times n \times m$. To reduce the amount of parameters for this stratification method, it was decided to only optimize the basal sliding $C$. Note that $C$ can only be inverted on those pixels that have observed ice thickness data available. This results in a sparse distribution of $C$ across the glacier area.

## 3.8 Complete Glacier Reconstruction

### 3.8.1 Nearest Neighbour Interpolation

To construct an ice thickness that covers the whole glacier region, the full basal sliding profile $C$ needs to be determined first. Therefore to obtain $C$ for each pixel, nearest neighbour interpolation is utilized. This carries several hypothesis, and it will introduce additional uncertainties to interpolated grid cells. Nonetheless, it was the simplest and most robust solution that could be found within the time frame of this thesis.

Nearest neighbor interpolation in a 2D image involves filling in a missing pixel value by directly copying the value of the nearest pixel. This process begins by identifying the pixel location where the value is missing. Then, the algorithm searches the surrounding pixels to find the closest one with a known value. The value from this nearest pixel is used to fill in the missing value in the image. This method is straightforward and does not involve any complex calculations, making it a quick and simple way to handle missing data in images. The interpolation can introduce step-like artifacts where the data changes abruptly from one pixel to its neighbor.

### 3.8.2 Gaussian Smoothing

Glaciers are inherently smooth and continuous entities. The basal sliding rates across a glacier's base are not likely to change abruptly in very short distances under natural conditions. Therefore to counter the artifacts introduced by interpolation, a Gaussian kernel is applied, which smoothens the solution. Gaussian kernel filtering averages data points by weighting neighboring points according to their distance, using a Gaussian function [53]. Mathematically this is:

$$G(x, y) = \frac{1}{2\pi\sigma^2} e^{-\left(\frac{x^2+y^2}{2\sigma^2}\right)} \tag{42}$$

In this research a 5x5 kernel, with $\sigma_{xy} = 1.0$, was used. Benchmarking the kernel specifics was not done, due to time constraints. The smoothing process applies a uniform filter across the data, potentially oversimplifying the complex, heterogeneous nature of the glacier bed. This oversimplification can lead to inaccurate representations of basal sliding mechanisms.

# 4 Results & Discussion

Throughout this section a specific glacier, cataloged as RGI60-11.01791 in the Central Europe region, is used to illustrate the nature of the data involved and the subsequent modeling outcomes. However this process was done for many glaciers, which will be discussed later on when showcasing aggregated results.

## 4.1 Available Observational Data

The used observed data encompasses the surface topography ($S$), ice thickness ($H$), and surface velocity ($V$), as is shown in the following figure for the example glacier:
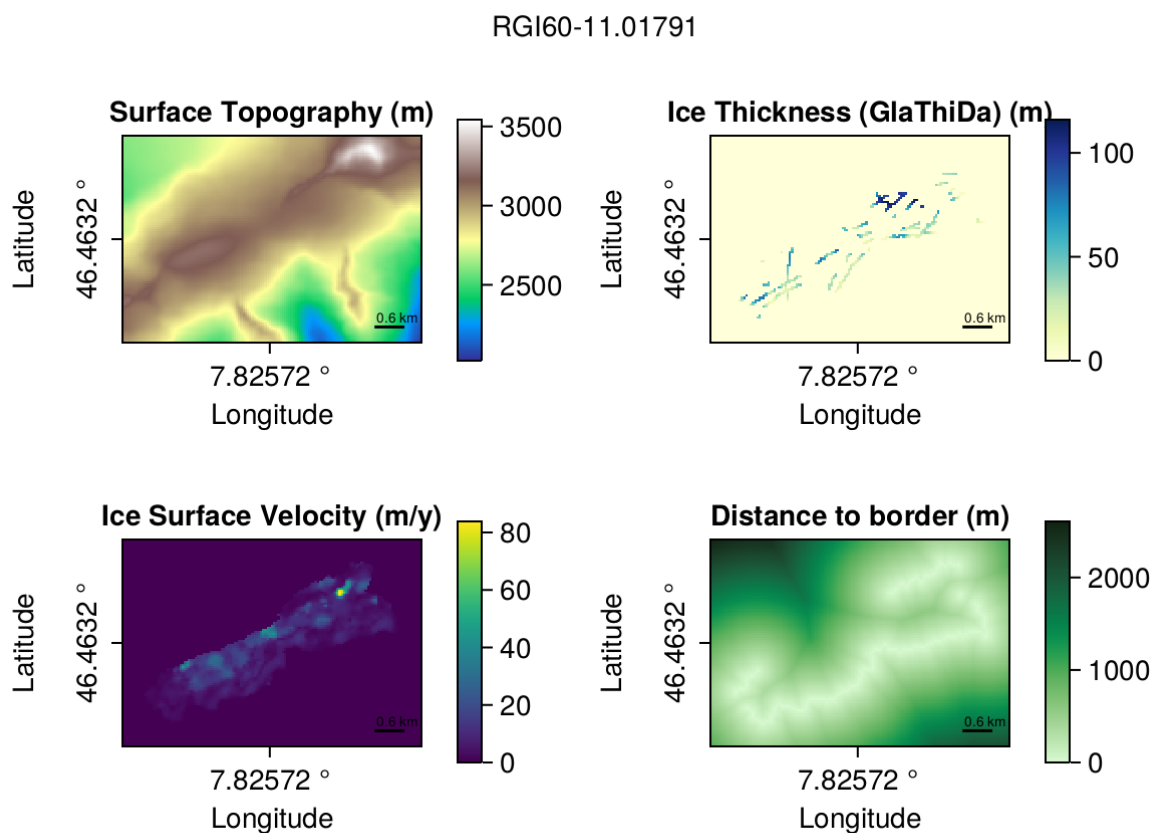


Figure 2: Observational data for the example glacier RGI60-11.01791. The top-left panel displays the surface topography, which depicts the glacier morphology. The top-right panel illustrates ice thickness data derived from the GlaThiDa database showing the glacier's spatial thickness distribution. The bottom-left panel presents remote sensing ice surface velocity measurements. The bottom-right panel shows the distance to the border of the glacier, essentially outlining the glacier shape. The glacier's geographical context is provided by the latitudinal and longitudinal coordinates.

The robustness and completeness of the available data are critical for guiding the inversion process towards an accurate estimation of parameters. In the original methodology, it was intended to dynamically propagate ice thickness over time using a forward model. This approach aimed to calculate glacier velocity from time-evolving ice thickness predictions, enabling a direct comparison with observed surface velocities. However, the limited availability and temporal resolution of ice thickness data from the GlaThiDa database necessitated a strategic pivot.

Due to these constraints, a steady-state assumption was adopted for the analysis, where it was assumed that the ice thickness remained nearly constant ($\frac{dh}{dt} \approx 0$) between the measurements of observed surface velocity and ice thickness. This assumption can be justified due to the slow and relatively stable nature of glacier dynamics over short to intermediate time scales, and also to the small contribution of surface mass balance to changing the ice thickness with respect to the total ice thickness of the glacier [54]. This adaptation made it possible to estimate ice thickness based on observed surface velocities, using Equation 35. This approach introduces several adjustable parameters related to glacier rheology, such as $A$, $n$, and $C$, which can be optimized. The optimized parameters can then be used to obtain an ice thickness that can be compared with the available sparse ice thickness measurements, providing a basis for model validation.

## 4.2   Single Glacier Model Performance

**Single Glacier Performance**

The analysis starts with looking at how single glaciers perform. For modeling, simple settings were used to match common temperate glacier conditions: $A = 7.57382 \times 10^{-17}$, and $n = 3$ [15]. The focus was on adjusting the basal sliding value $C$. The subject glacier was partitioned into 6x6 regions, delineating 36 distinct sectors based on elevation and distance to border. This resulted in the optimization of 36 unique parameters. The outcomes of this optimization are encapsulated in the Figures 3 & 4, illustrating the difference between observed and predicted ice thickness, as well as the spatial distribution of the basal sliding coefficient $C$.
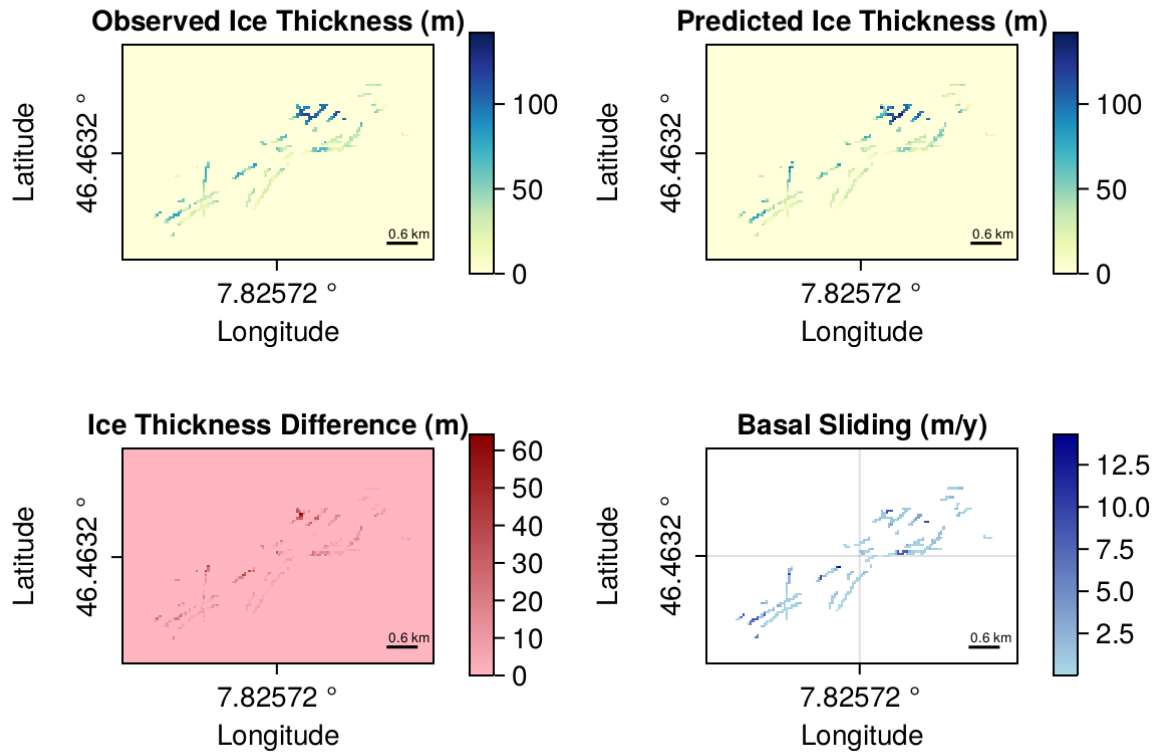
Figure 3: Top panels show the comparison of observed (left) and predicted (right) ice thickness across the glacier's surface, with flow model parameters $A = 7.57382 \times 10^{-17}$ s$^{-1}$Pa$^{-3}$ and $n = 3.0$. The bottom left panel illustrates the ice thickness differences between observed and predicted values, and the bottom right panel depicts the optimized basal sliding coefficient $C$.
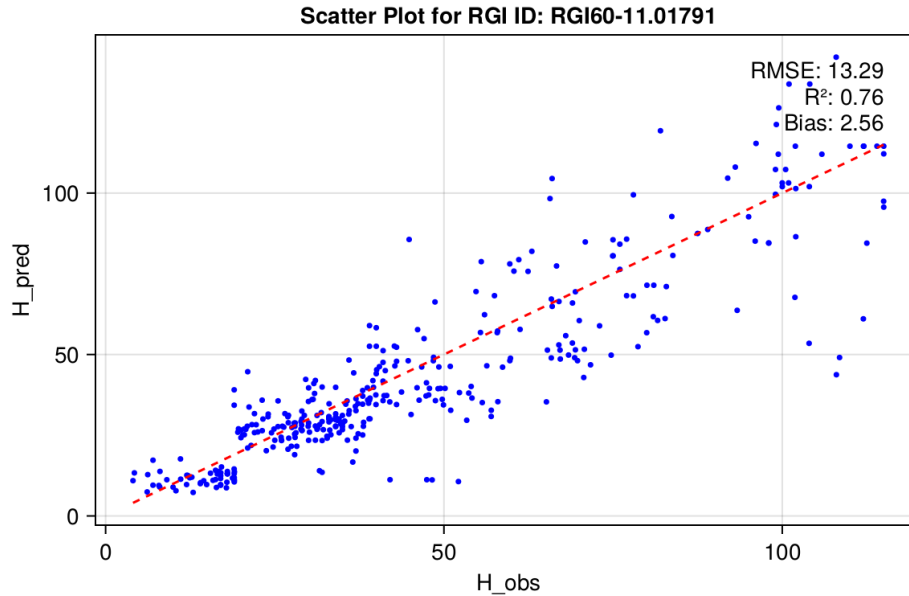
Figure 4: Scatter plot of predicted vs. observed ice thickness, with statistical metrics indicating the model's accuracy and bias.

There is a broad agreement between the observed and predicted ice thicknesses as is revealed in Figure 3. However, the difference map shows some sectors where the model diverges significantly from observed measurements, possibly pointing to areas with more intricate basal topography or areas where thermal regimes critically impact ice deformation rates. The uniform application of $A$ and $n$ across the glacier might oversimplify these behaviors, suggesting that the optimization of the basal sliding coefficient $C$ on itself is not enough. On the other hand advancing to a fully distributed inversion of the basal sliding coefficient $C$, rather than optimizing clustered area's, could better constrain many areas with specific behaviour. The scatter plot depicted in Figure 4 demonstrates a moderate level of predictive skill within the model, evidenced by a coefficient of determination ($R^2$) of 0.76. Despite this, the root mean square error (RMSE) of 13.29 m and the positive bias of 2.56 m highlight a systematic underestimation in the ice thickness predictions.

**Glacier Reconstruction**

To reconstruct the ice thickness, the basal sliding is reconstructed first using nearest neighbour interpolation and Gaussian smoothing. From this obtained distribution, the full ice thickness is inverted from the velocity data using the interpolated and smoothed $C$ values, allowing for a complete reconstruction of the glacier's thickness profile. All three elements are shown in Figure 5.
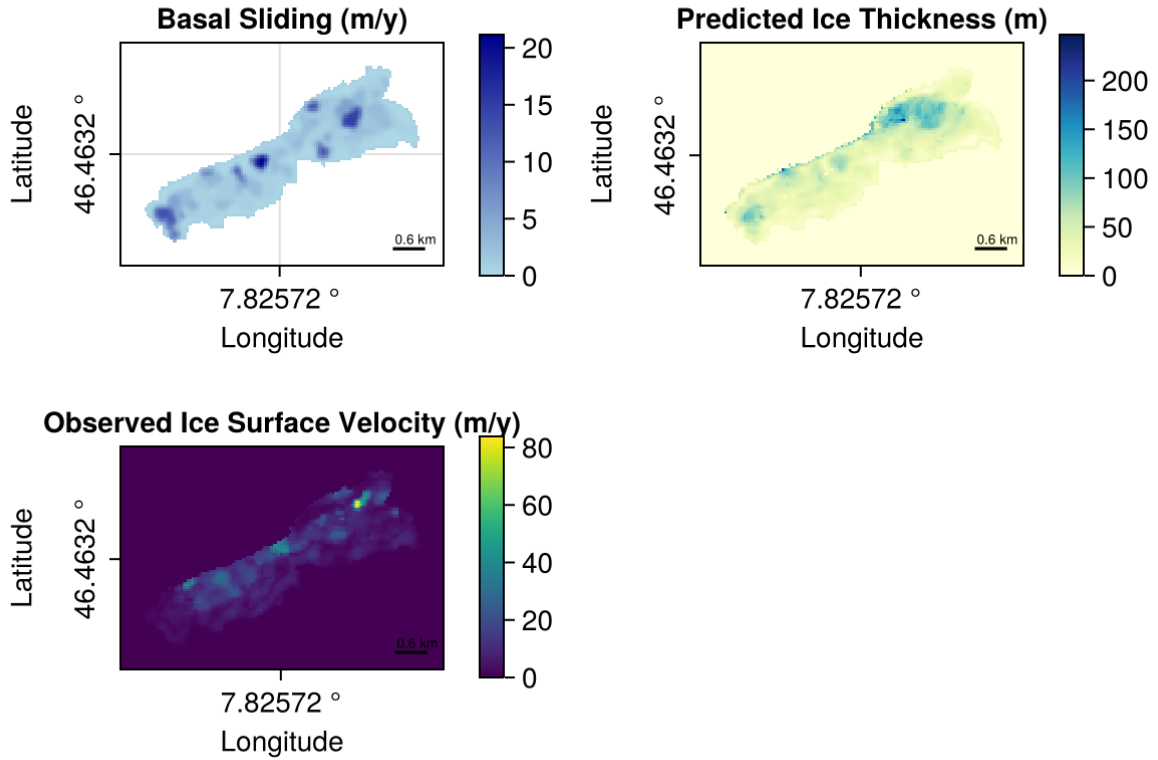
22

Figure 5: The left top panel displays the optimized basal sliding coefficient $C$ (left) that is interpolated based on observed surface velocity and slope, coupled with Gaussian kernel smoothing. The corresponding predicted ice thickness is shown in the top right panel. The bottom panel shows the observed ice surface velocity from which the inversion was done.

In Figure 5, the top left panel shows a basal sliding distribution that is unexpectedly even, but with some scattered values. Basal sliding should not be uniformly distributed across the glacier area. Instead, it should show variability that is influenced by a combination of factors like the temperature of the area, the slope of the glacier, the bed roughness, and the amount of meltwater from the glacier [15]. The non variability is probably caused by the fact that the method to retrieve the basal sliding, was not fully distributed. This leaves less space for imposing variability by interpolation methods. On the other hand basal sliding is expected to be more smooth and not vary to much within short distances. However abrupt changes can be seen. Therefore the used Gaussian kernel seems not sufficient here to impose the expected smoothness.

To further investigate the reconstructed ice thickness, a comparison is made with the inverted ice thickness from Farinotti et al. (2019) [44]. In Figure 6 the predicted ice thickness lacks the expected variations from the accumulation to ablation glacier regions, while this clearly can be seen in Figure 6. The reference image also shows more detail in the ice thickness variability, especially in the mid-section where there are distinct regions of thicker ice. The predicted thickness seems more uniform, which indicates that the natural variability of the

glacier's internal dynamics is not captured well. Furthermore the reference has a clear gradient of thickness, with a smoother transition from thick to thin ice. While the predicted ice thickness is to abrupt in places, not showing the gradual thinning that's expected from the central flow line to the margins. From this it is evident that nearest neighbour interpolation in combination with Gaussian smoothing, is not sufficient to retrieve a physically correct basal sliding and ice thickness for the whole glacier area.
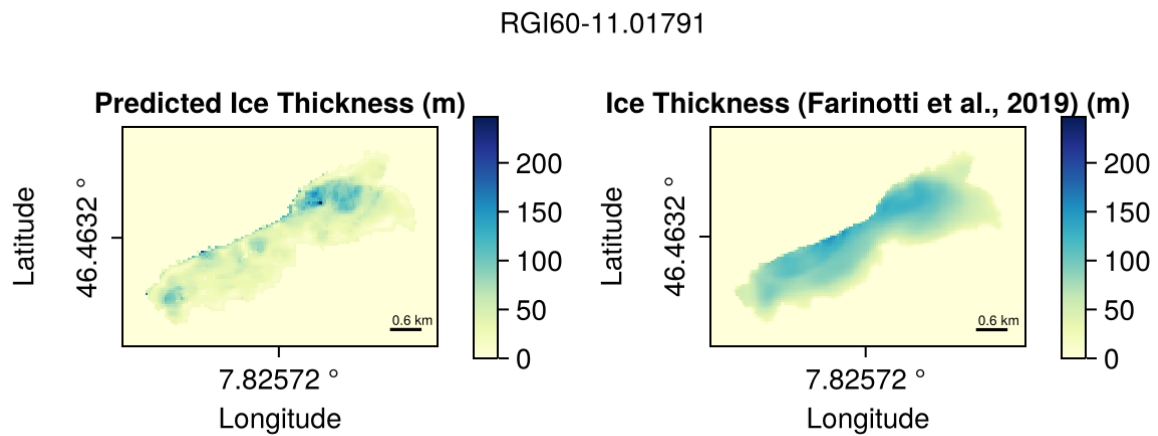


Figure 6: Comparison of predicted ice thickness vs inverted ice thickness from Farinotti et al. (2019).

## 4.3 Regional Glacier Model Performance

The analysis advances by evaluating the model's effectiveness across defined glacier regions. Within each region, optimization processes are performed for multiple glaciers, and the resulting metrics are aggregated. This allows for a comprehensive assessment of model performance at the regional level. The same specifications as in single glacier performance (see section 4.2), was used for each individual glacier. The investigated regions are:
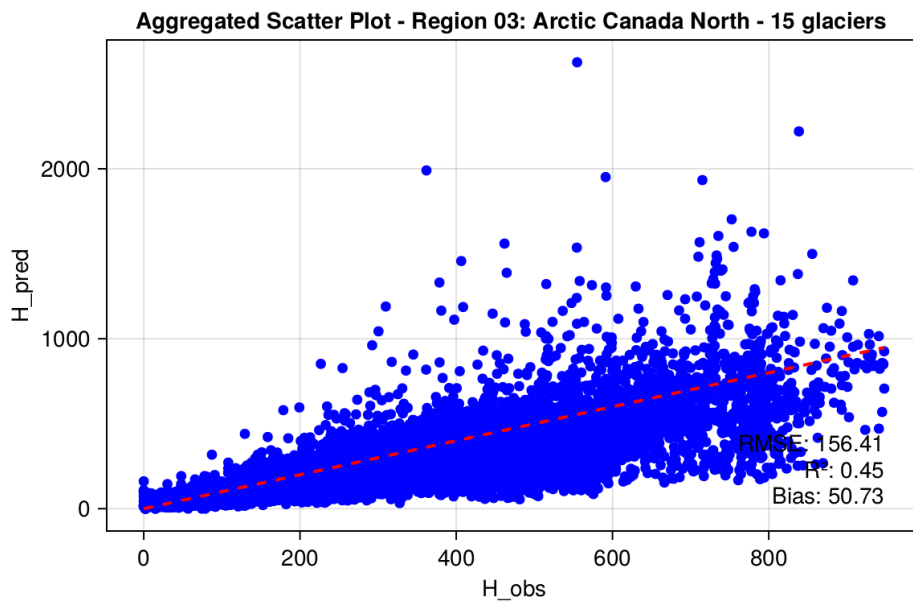
- Arctic Canada North

- Arctic Canada South

- Svalbard

- Central Europe

The selection of glaciers for each region was based on the availability of surface velocity measurements (Millan et al. (2022) [40]) and ice thickness data (GlaThiDa Consortium (2020) [41]). The full list of RGI60-IDs per region can be found in Appendix B.

Following the establishment of the selection criteria and regional categorization, a visual comparative analysis that illustrates the model's regional behavior is presented. In the forthcoming figures, not only the performance among the various regions are shown, but also the impact of spatial stratification on the predictive accuracy. For each region there are two aggregated scatter plots, corresponding to both stratified and non-stratified scenarios. In the non-stratified approach, a single set of parameters is optimized for an entire glacier; in this context, only the basal sliding coefficient $C$ is adjusted. Conversely, the stratified approach involves the optimization of 36 distinct $C$ parameters, each corresponding to different sectors within the glacier. This side-by-side presentation allows to gauge the stratification's efficacy and its role in model refinement.
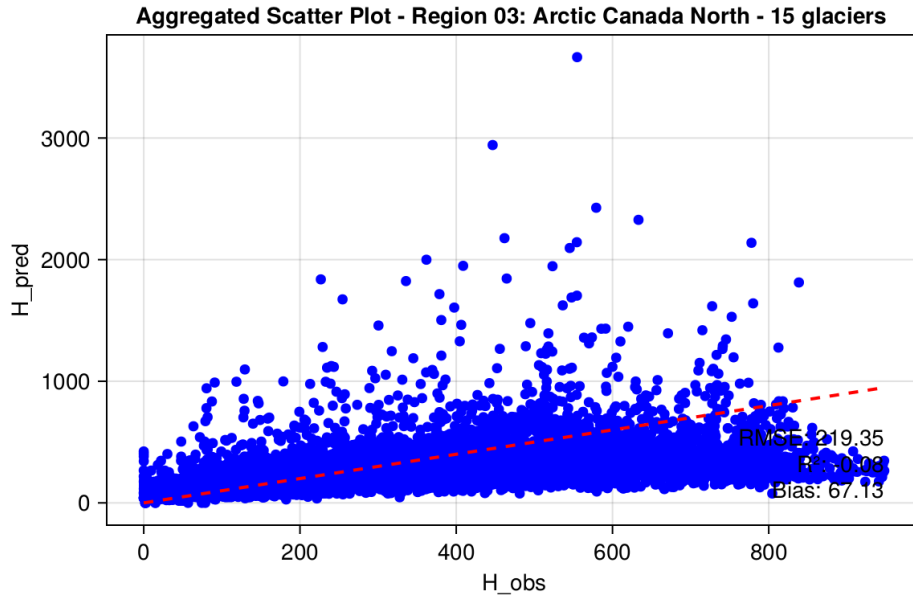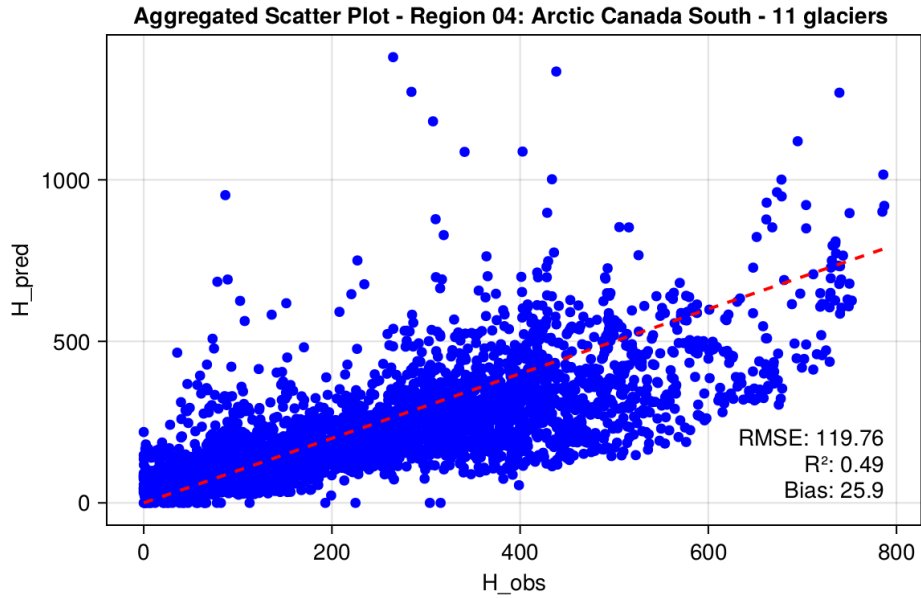
(a) No spatial stratification. Metrics: RMSE = 219.35, $R^2$ = -0.08, Bias = 67.13.
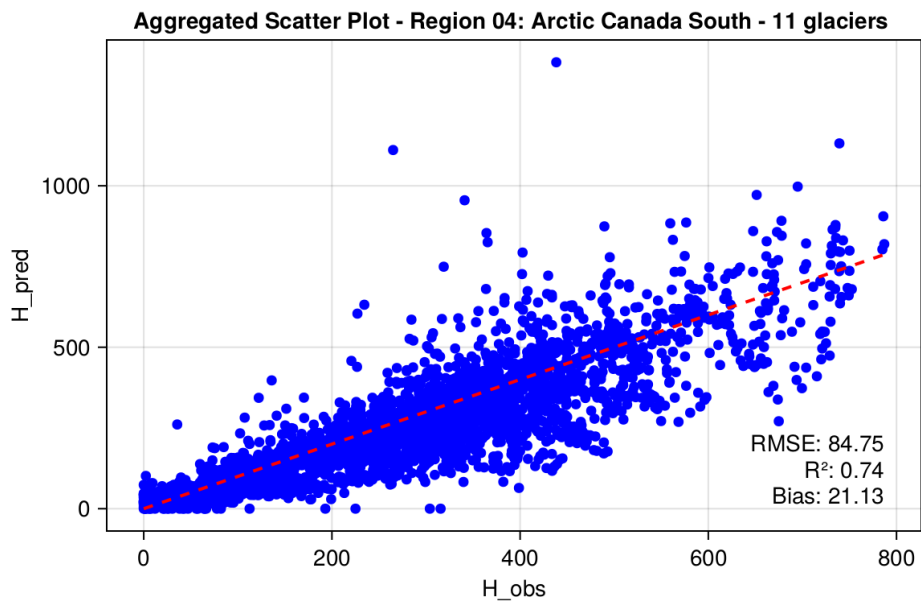


(b) With spatial stratification. Metrics: RMSE = 156.41, $R^2$ = 0.45, Bias = 50.73.

Figure 7: Comparison of aggregated scatter plots for the Arctic Canada North region, showing the relationship between observed and predicted ice thickness both without (upper) and with (lower) spatial stratification. The provided metrics illustrate the model's performance under each condition.

26

(a) No spatial stratification. Metrics: RMSE = 119.76, $R^2$ = 0.49, Bias = 25.9.



(b) With spatial stratification. Metrics: RMSE = 84.75, $R^2$ = 0.74, Bias = 21.13.

Figure 8: Comparison of aggregated scatter plots for the Arctic Canada South region, showing the relationship between observed and predicted ice thickness both without (upper) and with (lower) spatial stratification. The provided metrics illustrate the model's performance under each condition.
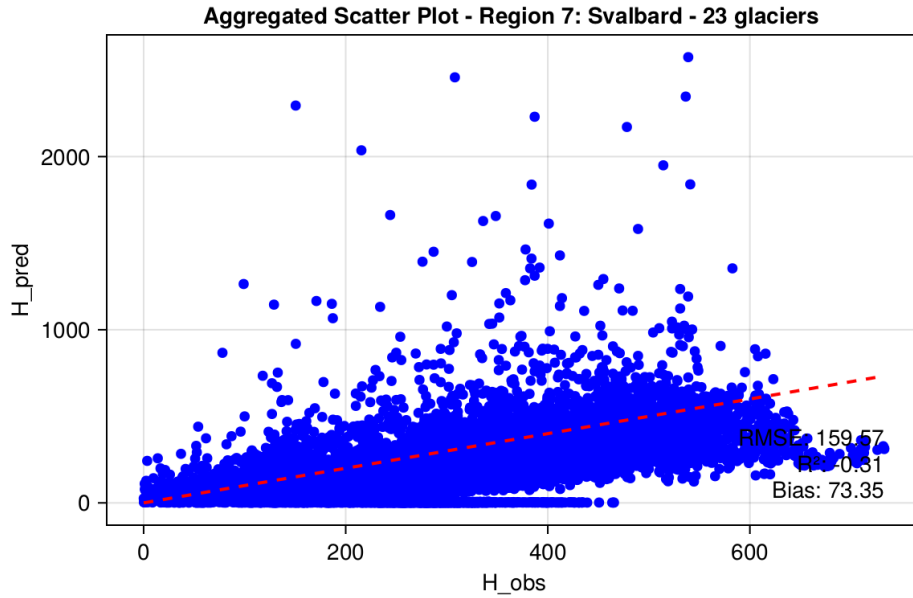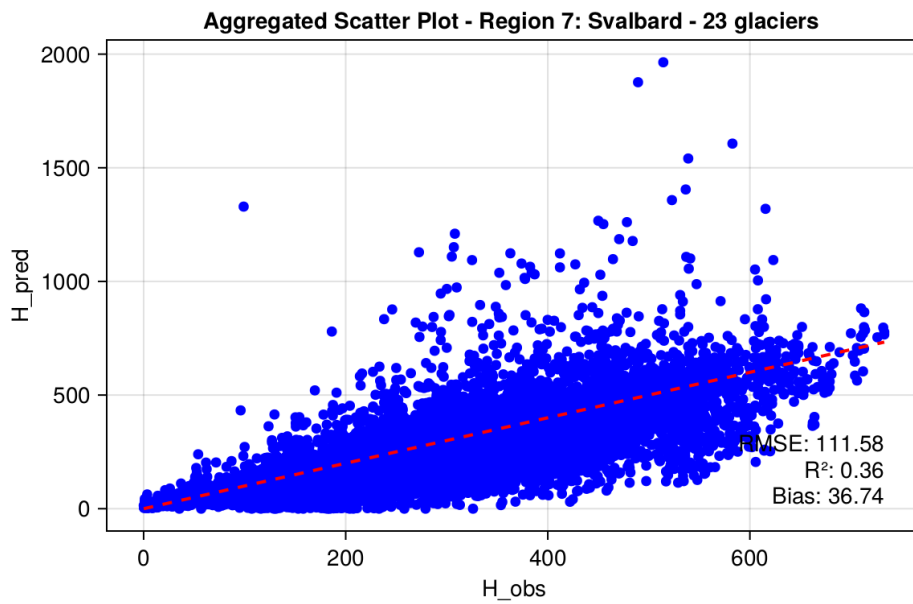
**Aggregated Scatter Plot - Region 7: Svalbard - 23 glaciers**

RMSE: 159.57
R²: -0.31
Bias: 73.35

(a) No spatial stratification. Metrics: RMSE = 159.57, $R^2$ = -0.31, Bias = 73.35.



**Aggregated Scatter Plot - Region 7: Svalbard - 23 glaciers**

RMSE: 111.58
R²: 0.36
Bias: 36.74

(b) With spatial stratification. Metrics: RMSE = 111.58, $R^2$ = 0.36, Bias = 36.74.

Figure 9: Comparison of aggregated scatter plots for the Svalbard, showing the relationship between observed and predicted ice thickness both without (upper) and with (lower) spatial stratification. The provided metrics illustrate the model's performance under each condition.
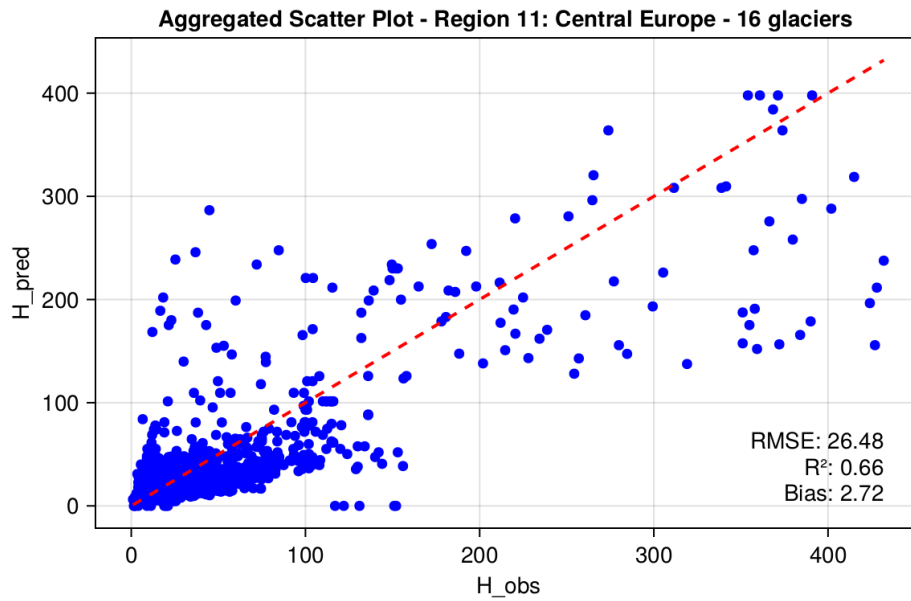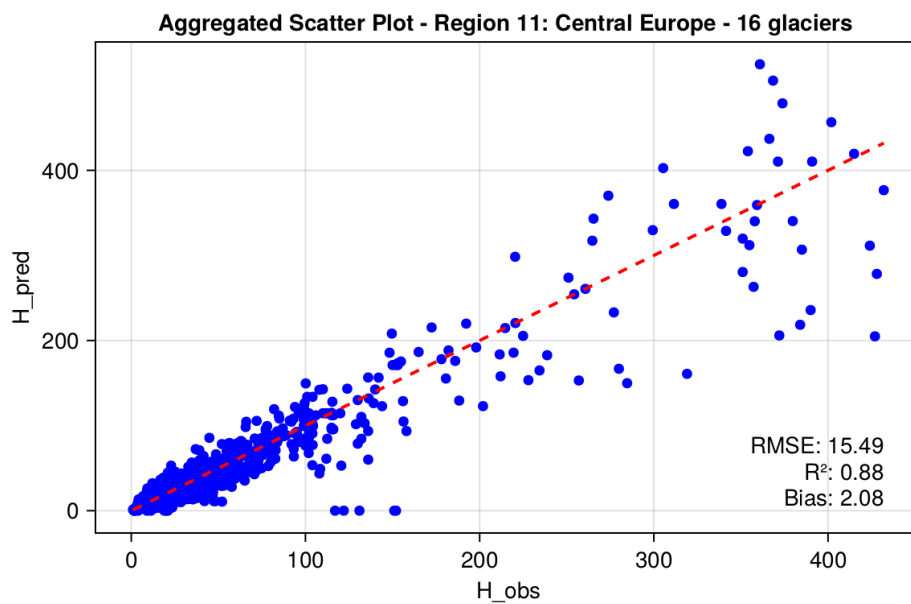
(a) No spatial stratification. RMSE = 26.48, $R^2$ = 0.66, Bias = 2.72.



(b) With spatial stratification. Metrics: RMSE = 15.49, $R^2$ = 0.88, Bias = 2.08.

Figure 10: Comparison of aggregated scatter plots for the Central Europe region, showing the relationship between observed and predicted ice thickness both without (upper) and with (lower) spatial stratification. The provided metrics illustrate the model's performance under each condition.

(a) Aggregated data without spatial stratification. Metrics: RMSE = 168.3, $R^2$ = 0.16, Bias = 58.35.



(b) Aggregated data with spatial stratification. Metrics: RMSE = 118.93, $R^2$ = 0.58, Bias = 35.52.

Figure 11: Comparison of aggregated scatter plots for all regions combined, showing the relationship between observed and predicted ice thickness both without (upper) and with (lower) spatial stratification. The provided metrics illustrate the model's performance under each condition.
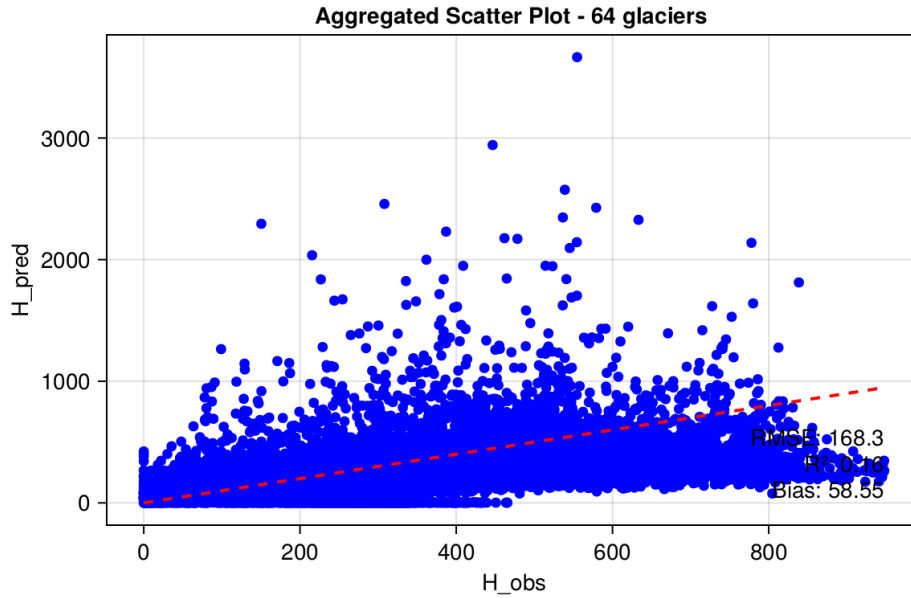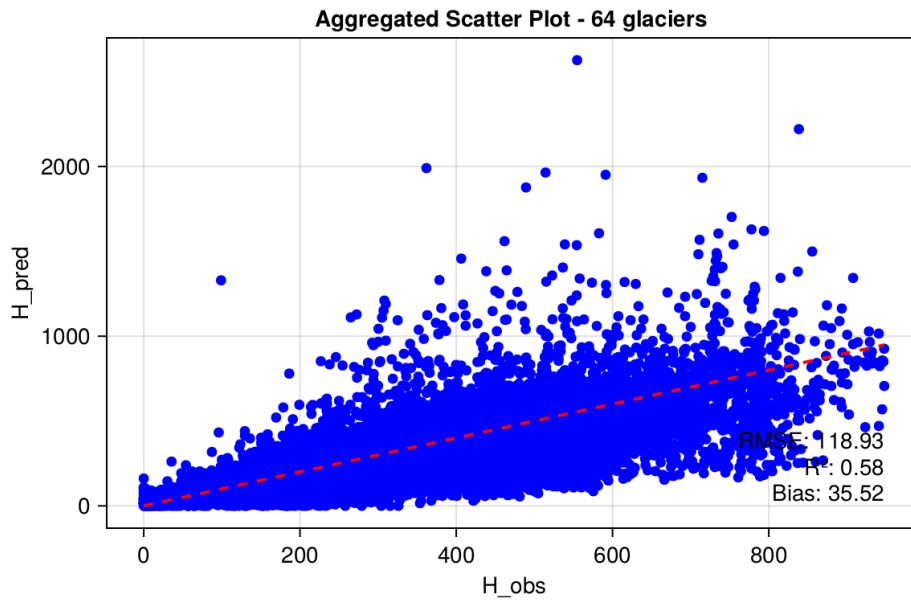
The scatter plots for the Arctic Canada North region (Figure 7) reveal a improvement in model performance with the introduction of spatial stratification. The negative R-squared value, initially indicating a lack of fit, is substantially improved to 0.45. Additionally, the reduction in RMSE from 219.35 to 156.41 and Bias from 67.13 to 50.73 indicates enhanced accuracy.

In the Arctic Canada South region (Figure 8), spatial stratification leads to a decrease in RMSE from 119.76 to 84.75 and an increase in R-squared from 0.49 to 0.74, confirming the method's effectiveness. A slight reduction in Bias further supports this observation.

For Svalbard (Figure 9), spatial stratification is transformative, turning a negative R-squared value into a positive one, up to 0.36. The RMSE is significantly lowered, and Bias shows an improvement, underlining the impact of considering spatial diversity in modeling efforts.

The Central Europe region (Figure 10) displays the most profound improvement with spatial stratification. The RMSE is substantially reduced, while the R-squared value reaches an impressive 0.88, indicating a very strong fit. The minimal decrease in Bias suggests that the predictions were reasonably accurate even before stratification.

The assumption of a temperate glacier regime ($A = 7.57382 \times 10^{-17}$), while mostly valid for the Central Europe, may not extend to the other regions. Because many glaciers are not necessarily temperate. This represents an additional uncertainty factor and could possibly explain why the performance in Central Europe is better, compared to the other regions.

The aggregation of scatter plot data from all regions (Figure 11) presents a holistic perspective on the model's performance, emphasizing the impact of spatial stratification on a larger scale. The combined data without spatial stratification shows a higher RMSE of 168.3 and a low R-squared value of 0.16, which indicates a relatively poor fit across the board. Upon applying spatial stratification, there is a noticeable improvement in the model's performance, with RMSE decreasing to 118.93 and R-squared increasing to 0.58, indicating a moderately strong correlation between observed and predicted values.

These insights underscore the crucial role of spatial stratification in regional glacier modeling, not only enhancing prediction accuracy, but also highlighting the importance of incorporating the spatial distribution of glacier rheology. Capturing the variability in rheological properties is essential for an accurate representation of observed glacier ice thickness and velocities. While spatial stratification appears to improve the model's fit, this method is not without its caveats. The slight reductions in Bias suggest that while the stratification fine-tunes the model to current observations, it may not account for the underlying processes driving glacier dynamics. Moreover, the R-squared values after stratification, although improved, do not reach a level of confidence that justifies the method.

## 4.4 Computational Efficiency and Julia's Role

The glacier inversion modeling conducted in this study leveraged the Julia programming language for its noted computational efficiency and extensive suite of scientific computing packages. Julia's prowess in handling complex numerical computations is essential for glacier dynamics modeling. For the inversion of all regions combined, a dataset involving 64 glaciers, the optimization procedure without spatial stratification took only 18 seconds for 64 parameters. When spatial stratification was introduced, the number of parameters increased to 2304 $(64 \times 36)$, which is a 36-fold increase. Despite this significant increase in the complexity of the problem, the completion time for the optimization only rose to 101 seconds. This corresponds to a time increase by a factor of approximately $5.6$, markedly lower than the parameter increase.

The efficiency of Julia's automatic differentiation, along with its multiprocessing capabilities, is reflected in the disproportionate fractional increase between computational time and the number of parameters. This demonstrates Julia's ability to manage large-scale optimizations with higher efficiency. Moreover, the interoperability of Julia with other languages ensures that it can be seamlessly integrated into existing workflows, further enhancing the productivity of glaciological research.

## 4.5 Methodological Reflections and Future Directions

The results shows the role of comprehensive data in securing the integrity of glacier models. Relying on steady-state assumptions and remote sensing glacier ice surface velocities was a crucial methodological decision. However, this decision also highlighted the inherent limitations of the available data. Such as the sparse measurements of ice thickness and lack of temporal diversity within both ice surface velocity and ice thickness. Spatial stratification has improved model performance and highlights the importance of incorporating the spatial distribution of glacier rheology, however it also brings to the forefront the need to balance computational cost with accuracy gains.

While the model has potential, the attempts at full glacier thickness reconstruction have not been entirely successful, because the predicted thickness did not show the typical variability that was expected. Therefore this area needs further investigation, for example by exploring geostatistical interpolation methods like Kriging Interpolation [55] and Inverse Distance Weighting (IDW) [56]. Kriging is a method that predicts unknown values by considering the spatial correlation of measurements, whereas IDW estimates values based on the weighted average of nearby data points, with closer points having more influence. Both methods are accessible within Julia using `GeoStats.jl` [57].

Future research must prioritize the exploration of more datasets and extend the database of ice velocities and ice thickness data. Advancing the models to account for the transient behaviors of glaciers will be crucial for capturing their true dynamics. Incorporating high-resolution temporal data, such as the surface velocity measurements by Nanni et al. (2023) [58], could be essential to enhance model accuracy, capture transient behaviour and enhance the reliability of its predictions. Future research should also aim for transitioning from Forward Mode AD to Reverse Mode AD to enhance computational efficiency, especially when integrating with a fully distributed inversion and temporal data. This combination is promising to create a model that fully comprehends the glacier rheology, while being as computationally efficient as possible.

# 5 Conclusion

The aim of this research was to deepenen our understanding of glacier dynamics through physics-based modeling, leveraging datasets of glacier surface velocities and ice thickness from satellite remote sensing. The study's core was to create a methodology to refine empirical laws for the two dimensional Shallow Ice Approximation, focusing on aspects like ice rheology and basal sliding, crucial for predicting glacier movements.

The integration of remote sensing data into glacier models has proven instrumental, allowing for more accurate calibration of these models. Despite challenges, such as the limitations posed by steady-state assumptions due to data scarcity, the study highlighted the critical role of high-quality, temporally resolved data in modeling glacier dynamics accurately.

Notably, the introduction of spatial stratification into the modeling process has marked a significant advancement, enhancing model performance with a notable reduction in Root Mean Square Error (RMSE) by up to 30% in certain regions and improving the coefficient of determination ($R^2$) values by as much as 0.2 to 0.4, depending on the region studied. Specifically, the need for models to capture the complex variability of glaciers more accurately was evident, pointing to the potential for fully distributed inversions.

This research underlines the importance of developing a model that deeply understands glacier rheology, using fully distributed inversions and temporal data. Where evolving from Forward to Reverse Mode Automatic Differentiation (AD) is crucial for computational efficiency. When inverting glacier characteristics (e.g. basal sliding) on sparse data, it is recommended to explore geostatistical interpolation methods to obtain these characteristics for the entire glacier area.

# References

[1] Sam Anderson and Valentina Radić. Identification of local water resource vulnerability to rapid deglaciation in alberta. *Nature Climate Change*, 10:933–938, 10 2020.

[2] B. Marzeion, A. H. Jarosch, and M. Hofer. Past and future sea-level change from the surface mass balance of glaciers. *The Cryosphere*, 6:1295–1322, 11 2012.

[3] Fiamma Straneo, Patrick Heimbach, Olga Sergienko, Gordon Hamilton, Ginny Catania, Stephen Griffies, Robert Hallberg, Adrian Jenkins, Ian Joughin, Roman Motyka, W. Pfeffer, Stephen Price, E. Rignot, Theodore Scambos, Martin Truffer, and Andreas Vieli. Challenges to understand the dynamic response of greenland's marine terminating glaciers to oceanic and atmospheric forcing. *Bulletin of the American Meteorological Society*, 94:1131–1144, 08 2013.

[4] Iliyana Dobreva, Michael Bishop, and Andrew Bush. Climate–glacier dynamics and topographic forcing in the karakoram himalaya: Concepts, issues and research directions. *Water*, 9:405, 6 2017.

[5] Stephen J. A. Jennings and Michael J. Hambrey. Structures and deformation in glaciers and ice sheets. *Reviews of Geophysics*, 59, 9 2021.

[6] B. Orlove. Glacier retreat: Reviewing the limits of human adaptation to climate change. *Environment*, 51:22–34, 05 2009.

[7] J. Oerlemans. *Glaciers and Climate Change*. A. A. Balkema Publishers, 2001.

[8] R. LeB. Hooke. *Principles of Glacier Mechanics (2nd ed.)*. Cambridge University Press, 2005.

[9] G. K. C. Clarke. Subglacial processes. *Annual Review of Earth and Planetary Sciences*, 33:247–276, 2005.

[10] A. Hubbard and N. Glasser. *Field Techniques in Glaciology and Glacial Geomorphology*. John Wiley and Sons, 2005.

[11] S. Solomon et al. *Climate Change 2007: The Physical Science Basis*. Cambridge University Press, 2007.

[12] J. E. Box et al. Greenland ice sheet albedo feedback: thermodynamics and atmospheric drivers. *The Cryosphere*, 6:821–839, 2012.

[13] Jordi Bolibar, Antoine Rabatel, Isabelle Gouttevin, Harry Zekollari, and Clovis Galiez. Nonlinear sensitivity of glacier mass balance to future climate change unveiled by deep learning. *Nature Communications*, 13, 12 2022.

[14] K. Hutter. *Theoretical Glaciology: Material Science of Ice and the Mechanics of Glaciers and Ice Sheets*. Mathematical Approaches to Geophysics. Springer, 1983.

[15] K. M. Cuffey and W. S. B. Paterson. *The Physics of Glaciers (4th ed.)*. Academic Press, 2010.

[16] V. F. Petrenko and R. W. Whitworth. *Physics of Ice*. Oxford University Press, 1999.

[17] A. C. Fowler and D. A. Larson. On the flow of polythermal glaciers - i. model and preliminary analysis. *Proceedings of the Royal Society of London. A. Mathematical and Physical Sciences*, 363:217–242, 1978.

[18] V. Uruba. On reynolds number physical interpretation. In *AIP Conference Proceedings*, volume 2000, page 020019, 2018.

[19] A. C. Fowler. Glaciers and ice sheets. In *The Mathematics of Models for Climatology and Environment*, pages 301–336. Springer Berlin Heidelberg, 1997.

[20] Fowler A. and Ng F. *Glaciers and Ice Sheets in the Climate System*. Springer International Publishing, 2021.

[21] Ralf Greve. Dynamics of ice sheets and glaciers. 2004.

[22] J. Weertman. On the sliding of glaciers. *Journal of Glaciology*, 3:33–38, 1957.

[23] W. Michael Lai, David Rubin, and Erhard Krempl. Chapter 7 - the reynolds transport theorem and applications. In W. Michael Lai, David Rubin, and Erhard Krempl, editors, *Introduction to Continuum Mechanics (Fourth Edition)*, pages 411–441. Butterworth-Heinemann, Boston, fourth edition edition, 2010.

[24] Frank E. Harris. Chapter 7 - vector analysis. In Frank E. Harris, editor, *Mathematics for Physical Science and Engineering*, pages 229–292. Academic Press, Boston, 2014.

[25] Theodore L. Bergman. *Fundamentals of heat and mass transfer*. J. Wiley amp; Sons, 2011.

[26] Glen J.W. The creep of polycrystalline ice. *Proceedings of the Royal Society of London. Series A. Mathematical and Physical Sciences*, 228:519–538, 1955.

[27] M. D. Behn, D. L. Goldsby, and G. Hirth. The role of grain size evolution in the rheology of ice: implications for reconciling laboratory creep data and the glen flow law. *The Cryosphere*, 15(9):4589–4605, 2021.

[28] Daniela Jansen, Henner Sandhäger, and Wolfgang Rack. Model experiments on large tabular iceberg evolution: Ablation and strain thinning. *Journal of Glaciology*, 51:363–372, 06 2005.

[29] Christian Schoof and Ian Hewitt. Ice-sheet dynamics. *Annual Review of Fluid Mechanics*, 45(1):217–239, 2013.

[30] Nina Kirchner, Kolumban Hutter, Martin Jakobsson, and Richard Gyllencreutz. Capabilities and limitations of numerical ice sheet models: a discussion for earth-scientists and modelers. *Quaternary Science Reviews*, 30(25):3691–3704, 2011.

[31] Zhihua Zhang and John C. Moore. Chapter 13 - glaciers and sea level rise. In Zhihua Zhang and John C. Moore, editors, *Mathematical and Physical Fundamentals of Climate Change*, pages 441–455. Elsevier, Boston, 2015.

[32] Jordi Bolibar, Facundo Sapienza, Fabien Maussion, Redouane Lguensat, Bert Wouters, and Fernando Pérez. Universal differential equations for glacier ice flow modelling. *GMD*, 2023.

[33] Christopher Rackauckas, Yingbo Ma, Julius Martensen, Collin Warner, Kirill Zubov, Rohit Supekar, Dominic Skinner, Ali Ramadhan, and Alan Edelman. Universal differential equations for scientific machine learning, 2021.

[34] F. Maussion, A. Butenko, N. Champollion, M. Dusch, J. Eis, K. Fourteau, P. Gregor, A. H. Jarosch, J. Landmann, F. Oesterle, B. Recinos, T. Rothenpieler, A. Vlug, C. T. Wild, and B. Marzeion. The open global glacier model (oggm) v1.1. *Geoscientific Model Development*, 2019:909–931, 2019.

[35] Jeff Bezanson, Alan Edelman, Stefan Karpinski, and Viral B. Shah. Julia: A fresh approach to numerical computing. *CoRR*, abs/1411.1607, 2014.

[36] Jarrett Revels, Miles Lubin, and Theodore Papamarkou. Forward-mode automatic differentiation in julia. *CoRR*, abs/1607.07892, 2016.

[37] Christopher Rackauckas, Mike Innes, Yingbo Ma, Jesse Bettencourt, Lyndon White, and Vaibhav Dixit. Diffeqflux.jl - A julia library for neural differential equations. *CoRR*, abs/1902.02376, 2019.

[38] Vaibhav Kumar Dixit and Christopher Rackauckas. Optimization.jl: A unified optimization package, March 2023.

[39] Simon Danisch and Julius Krumbiegel. Makie.jl: Flexible high-performance data visualization for Julia. *Journal of Open Source Software*, 6(65):3349, 2021.

[40] Romain Millan, Jérémie Mouginot, Antoine Rabatel, and Mathieu Morlighem. Ice velocity and thickness of the world's glaciers. *Nature Geoscience*, 15:124–129, 2 2022.

[41] GlaThiDa Consortium. Glacier thickness database 3.1.0, 2020. DOI: 10.5904/wgms-glathida-2020-10.

[42] A. Jarvis, Hannes Reuter, Andy Nelson, and Edith Guevara. Hole-filled seamless srtm data v4. tech. rep., international centre for tropical agriculture (ciat). *Cali, Columbia*, 01 2008.

[43] Jonathan de Ferranti. Digital Elevation Data from Viewfinder Panoramas. `https://viewfinderpanoramas.org/dem3.html`, 2022. Last revision 15 May 2022. Current work in progress.

[44] Daniel Farinotti, Matthias Huss, Johannes J. Fürst, Johannes Landmann, Horst Machguth, Fabien Maussion, and Ankur Pandit. A consensus estimate for the ice thickness distribution of all glaciers on earth. *Nature Geoscience*, 12:168–173, 3 2019.

[45] Timothy O. Hodson, Thomas M. Over, and Sydney S. Foks. Mean squared error, deconstructed. *Journal of Advances in Modeling Earth Systems*, 13, 12 2021.

[46] Sergio Bermejo and Joan Cabestany. Oriented principal component analysis for large margin classifiers. *Neural Networks*, 14(10):1447–1461, 2001.

[47] Roger Fletcher. *Practical Methods of Optimization*. John Wiley & Sons, New York, NY, USA, second edition, 1987.

[48] Xiangrong Li. A limited memory bfgs subspace algorithm for bound constrained nonsmooth problems. *Journal of Inequalities and Applications*, 2020:135, 12 2020.

[49] A. Griewank and A. Walther. *Evaluating Derivatives: Principles and Techniques of Algorithmic Differentiation, Second Edition*. Other Titles in Applied Mathematics. Society for Industrial and Applied Mathematics, 2008.

[50] Birthe van den Berg, Tom Schrijvers, James McKinna, and Alexander Vandenbroucke. Forward- or reverse-mode automatic differentiation: What's the difference?, 12 2022.

[51] Johnson Agbinya. *Calculus on Computational Graphs - an Introduction*. 02 2021.

[52] Deniz Oktay, Nick McGreivy, Joshua Aduol, Alex Beatson, and Ryan P. Adams. Randomized automatic differentiation, 2021.

[53] Moo K. Chung. Gaussian kernel smoothing, 2021.

[54] O. V. Sergienko. Marine outlet glacier dynamics, steady states and steady-state stability. *Journal of Glaciology*, pages 1–15, 3 2022.

[55] Donald E. Myers. Kriging, cokriging, radial basis functions and the role of positive definiteness. *Computers & Mathematics with Applications*, 24(12):139–148, 1992.

[56] Donald S. Shepard. A two-dimensional interpolation function for irregularly-spaced data. *Proceedings of the 1968 23rd ACM national conference*, 1968.

[57] Júlio Hoffimann, Fredrik Ekre, Martijn Visser, Anshul Singhvi, Durand D'souza, M. A. Siddique, Morten Piibeleht, Tony Kelman, and Zlatan Vasović. Juliaearth/geostats.jl: v0.11.7, June 2020.

[58] Ugo Nanni, Dirk Scherler, Francois Ayoub, Romain Millan, Frederic Herman, and Jean-Philippe Avouac. Climatic control on seasonal variations in mountain glacier surface velocity. *The Cryosphere*, 17:1567–1583, 4 2023.

# Appendix A: Derivation of the Advection-Diffusion Equation

Given the energy conservation equation:

$$\frac{d}{dt}\int_V \rho\left(e + \frac{1}{2}|\boldsymbol{u}|^2\right)dV = -\int_{\partial V}\rho\left(e + \frac{1}{2}|\boldsymbol{u}|^2\right)\boldsymbol{u}\cdot\boldsymbol{n}dS$$

$$+\int_{\partial V}k\nabla T\cdot\boldsymbol{n}dS$$

$$+\int_V\rho\boldsymbol{u}\cdot\boldsymbol{g}dV$$

$$+\int_{\partial V}\boldsymbol{u}\cdot(\boldsymbol{\tau}\cdot\boldsymbol{n})dS.$$

Start by omitting the kinetic energy terms $|u|^2$ as they are very small compared to the internal energy term $e$ [15] [20].

Using the Reynolds transport theorem:

$$\frac{d}{dt}\int_V \rho e\,dV = \int_V \rho\frac{De}{Dt}dV + \int_V e\frac{D\rho}{Dt}dV$$

Transforming the surface integrals to volume integrals using the divergence theorem:

$$\int_{\partial V}\rho e\boldsymbol{u}\cdot\boldsymbol{n}dS = \int_V \nabla\cdot(\rho e\boldsymbol{u})dV$$

$$\int_{\partial V}k\nabla T\cdot\boldsymbol{n}dS = \int_V \nabla\cdot(k\nabla T)dV$$

$$\int_{\partial V}\boldsymbol{u}\cdot(\boldsymbol{\tau}\cdot\boldsymbol{n})dS = \int_V \nabla\cdot(\boldsymbol{u}\cdot\boldsymbol{\tau})dV$$

Equating all the volume integrals:

$$\int_V \rho\frac{De}{Dt}dV + \int_V e\frac{D\rho}{Dt}dV = \int_V \nabla\cdot(\rho e)\boldsymbol{u}dV + \int_V \nabla\cdot(k\nabla T)dV + \int_V \rho\boldsymbol{u}\cdot\boldsymbol{g}dV + \int_V \nabla\cdot(\boldsymbol{u}\cdot\boldsymbol{\tau})dV$$

Given the thermodynamic relation:

$$\frac{De}{Dt} = c_p\frac{DT}{Dt} \implies \int_V \rho\frac{De}{Dt}dV = \int_V \rho c_p\frac{DT}{Dt}dV$$

Using the continuity equation:

$$\frac{\partial \rho}{\partial t} = -\nabla \cdot (\rho \boldsymbol{u})$$

the material derivative of the density can be expressed as:

$$\frac{D\rho}{Dt} = \frac{\partial \rho}{\partial t} + \boldsymbol{u} \cdot \nabla \rho$$

Substituting in the given continuity equation gives:

$$\frac{D\rho}{Dt} = \boldsymbol{u} \cdot \nabla \rho - \nabla \cdot (\rho \boldsymbol{u})$$

Now, substituting these relations into the energy conservation equation:

$$\int_V \rho c_p \frac{DT}{Dt} dV + \int_V e \left( \boldsymbol{u} \cdot \nabla \rho - \nabla \cdot (\rho \boldsymbol{u}) \right) dV$$
$$= \int_V \nabla \cdot (\rho e \boldsymbol{u}) dV + \int_V \nabla \cdot (k \nabla T) dV + \int_V \rho \boldsymbol{u} \cdot \boldsymbol{g} dV$$
$$+ \int_V \nabla \cdot (\boldsymbol{u} \cdot \boldsymbol{\tau}) dV$$

By equating the integrands, the differential form of the energy conservation equation is:

$$\rho c_p \frac{DT}{Dt} + e \left( \boldsymbol{u} \cdot \nabla \rho - \nabla \cdot (\rho \boldsymbol{u}) \right) = \nabla \cdot (\rho e \boldsymbol{u}) + \nabla \cdot (k \nabla T) + \rho \boldsymbol{u} \cdot \boldsymbol{g} + \nabla \cdot (\boldsymbol{u} \cdot \boldsymbol{\tau})$$

In the case of incompressible flow, $\nabla \rho$, $\frac{\partial \rho}{\partial t} = 0 \implies \nabla \cdot \boldsymbol{u} = 0$ and $\nabla e = 0$ (negligible spatial variation of internal energy), which leads to:

$$\rho c_p \left( \frac{\partial T}{\partial t} + \boldsymbol{u} \cdot \nabla T \right) = \nabla \cdot (k \nabla T) + \rho \boldsymbol{u} \cdot \boldsymbol{g} + \tau_{ij} \dot{\epsilon}_{ij}$$

Note that $\boldsymbol{u} \cdot \boldsymbol{g} = u_z g$. This term is very small as the vertical velocity is smaller than the horizontal velocity for ice flow (total velocity is already very slow). Thus the advection-diffusion equation for the temperature is acquired:

$$\rho c_p \left( \frac{\partial T}{\partial t} + \boldsymbol{u} \cdot \nabla T \right) = \nabla \cdot (k \nabla T) + \tau_{ij} \dot{\epsilon}_{ij}.$$

# Appendix B : RGI60-IDs of glaciers per region

## Region 03: Arctic Canada North

RGI60-03.00389, RGI60-03.01641, RGI60-03.00419, RGI60-03.01644,
RGI60-03.01742, RGI60-03.02429, RGI60-03.01687, RGI60-03.04538,
RGI60-03.00093, RGI60-03.02442, RGI60-03.00085, RGI60-03.01744,
RGI60-03.02468, RGI60-03.00109, RGI60-03.00108

## Region 04: Arctic Canada South

RGI60-04.06852, RGI60-04.05370, RGI60-04.05553, RGI60-04.05755,
RGI60-04.05746, RGI60-04.05776, RGI60-04.05372, RGI60-04.05765,
RGI60-04.05745, RGI60-04.05639, RGI60-04.05514

## Region 07: Svalbard

RGI60-07.01482, RGI60-07.00428, RGI60-07.01065, RGI60-07.01466,
RGI60-07.00608, RGI60-07.00028, RGI60-07.00551, RGI60-07.00681,
RGI60-07.01499, RGI60-07.00727, RGI60-07.01474, RGI60-07.00552,
RGI60-07.01449, RGI60-07.01470, RGI60-07.00423, RGI60-07.00425,
RGI60-07.00728, RGI60-07.00296, RGI60-07.00607, RGI60-07.00424,
RGI60-07.01477, RGI60-07.01472, RGI60-07.00301

## Region 11: Central Europe

RGI60-11.01450, RGI60-11.00638, RGI60-11.03247, RGI60-11.03248,
RGI60-11.01376, RGI60-11.02600, RGI60-11.01813, RGI60-11.00590,
RGI60-11.01791, RGI60-11.00950, RGI60-11.00695, RGI60-11.01790,
RGI60-11.01473, RGI60-11.01024, RGI60-11.00846, RGI60-11.00996